ADVANCED ENGINEERING MATERIALS
www.aem-journal.com

Preliminary Evaluation of the Influence of Hydrogen on the Fracture Toughness of an X65 Gas-Transmission Pipeline Steel

*Md Fahdul Wahab Chowdhury, Clotario V. Tapia-Bastidas, Joshua Hoschke, Jeffrey Venezuela, Ting Liu, Milos B. Djukic, Tom Depover, Kim Verbeken, Lenny Mcinnes, Maximilian Roethig, Amir Karimi, and Andrej Atrens**

Previous research has indicated that hydrogen decreases the fracture toughness of gas-transmission pipeline steels. This study produced two values of fracture toughness for the X65 steel in the Dampier Bunbury natural gas-transmission pipeline in air (J_Q of 590 and 778 kJ m^{-2}; equivalent to K_Q of 369 and 487 MPa$\sqrt{m}$) and two essentially American Society for Testing of Materials–valid values of fracture toughness of K_{J1C} of 150 and 189 MPa$\sqrt{m}$ for X65 subjected to in situ hydrogen charging thought to be equivalent to a hydrogen gas pressure of 200 bar. The fracture toughness for hydrogen-charged specimens was lower than in air. The large spread of the fracture toughness in air was attributable to the fact that these J_Q values were dependent on testing details. The spread of fracture toughness values in hydrogen was attributed to the variability of fracture toughness in hydrogen under these hydrogen-charging conditions. There was considerable stable crack growth. The energy for stable crack growth increased with crack length. The fractography in the presence of hydrogen showed significant ductility, consistent with hydrogen-assisted plastic fracture. The values of fracture toughness in air and with hydrogen were consistent with literature values.

1. Introduction

1.1. Hydrogen Embrittlement

Hydrogen is an energy carrier that can be transported using existing natural gas transmission pipelines from locations where green hydrogen can be generated using wind and solar to the destinations where hydrogen is utilized. Hydrogen dissolved in the steel may cause hydrogen embrittlement (HE): the reduction of mechanical strength, ductility, and fracture toughness.[1–11] Prior research has indicated that relevant hydrogen concentrations decrease the strength somewhat but significantly reduce the fracture toughness and ductility of pipeline steel. Safe pipeline operation therefore requires determination of tolerable defect sizes and permissible safe operating pressures for gas pipelines carrying hydrogen. Gas pipeline steels are standardized by the American Petroleum Institute (API) standard API 5 L. Examples are X42, X52, X65, X70, X80, and X100. Pipeline steels are produced to a strength criterion. Consequently, different pipeline steels (and pipeline steels manufactured to a particular API specification) may have significantly different microstructures and different susceptibilities to HE. Prior research[12–34] has addressed HE mechanisms and the influence of steel microstructure and chemical composition.

Typical pipeline steels, X52, X65, and X70, were shown to have decreasing fracture toughness with increasing hydrogen concentration as introduced by a higher cathodic charging current

M. F. W. Chowdhury, C. V. Tapia-Bastidas, J. Hoschke, J. Venezuela, T. Liu, L. Mcinnes, M. Roethig, A. Karimi, A. Atrens
School of Mechanical and Mining Engineering
Centre for Advanced Materials Processing and Manufacturing (AMPAM)
The University of Queensland
St. Lucia, Queensland 4072, Australia
E-mail: andrejs.atrens@uq.edu.au

The ORCID identification number(s) for the author(s) of this article can be found under https://doi.org/10.1002/adem.202400352.

DOI: 10.1002/adem.202400352

C. V. Tapia-Bastidas
Escuela Superior Politécnica Del Litoral – Espol
Guayaquil EC090150, Ecuador

M. B. Djukic
Faculty of Mechanical Engineering
University of Belgrade
Kraljice Marije 16, Belgrade 11120, Serbia

T. Depover, K. Verbeken
Department of Materials
Textiles and Chemical Engineering
Ghent University
Technologiepark 46, B-9052 Ghent, Belgium

density by Chatzidouros et al.[19] Subsequently, Chatzidouros et al.[18] found that the fracture toughness of X65 had a greater hydrogen-induced fracture toughness reduction than X52 and X70. Similarly, Kyriakopoulou et al.[25] found that hydrogen decreased the fracture toughness of X65, and Chatzidouros et al.[17,20] found that hydrogen decreased the fracture toughness of X42, X52, X65, and X70, with X65 having the largest decrease.

Fracture toughness decreases with increasing in situ hydrogen-charging current density were also measured for different steel grades by Xu et al.[35] Guy and Capelle,[36] and Hoyos et al.[37] Xu et al.[35] measured decreasing fracture toughness for X65 in terms of the *CTOD* with increasing in situ hydrogen charging at 1, 2, 4, and 8 mA cm^{-2} current density in simulated soil solution. The *CTOD* value decreased for the base metal (BM) and weld metal (WM) with increasing current density, with the WM showing the greater decrease.

Similarly, Xu[38] found that the fracture toughness of carbon steels (including pipeline steels) decreased when exposed to high-pressure gaseous hydrogen. The fracture toughness of the pipeline steels X42, X52, X60, X70, and X80 exposed to 6.9 MPa gaseous hydrogen ranged from 95 to 111 MPa$\sqrt{m}$. X80 had a fracture toughness of 105 MPa$\sqrt{m}$ exposed to 13.8 MPa gaseous hydrogen.

Stalheim et al.[39] and San Marchi et al.[40] measured the fracture toughness of pipeline steels X80 and X65 in hydrogen pressure at 5.5 and 21 MPa. The fracture toughness tests in hydrogen met the size requirement for the plane strain fracture toughness (J_{IC}) but did not meet the requirement of a uniform crack front. The measured fracture toughness for X80, designated as K_Q, at the hydrogen pressures 5.5 and 21 MPa, was 105 and 102 MPa$\sqrt{m}$, respectively. K_Q at hydrogen pressures of 5.5 MPa and 21 MPa for X60 was 85 MPa$\sqrt{m}$ and 82 MPa$\sqrt{m}$, respectively.

Lam et al.[41] reviewed the fracture toughness of pipeline steels. The fracture toughnesses of A516 grade 70 steel measured by Robinson and Stoltz[42] in air and in hydrogen at pressures of 3.5, 6.9, 20.7, and 34.5 MPa were 150, 119, 102, 89, and 82 MPa$\sqrt{m}$, respectively. The fracture toughness of steel similar to X42 was measured by Gutierrez-Solana and Elices[43] at hydrogen pressures of 0, 2, 4, and 6.5 MPa using three point bending to be 147, 128/101, 85, and 69 MPa$\sqrt{m}$. Duncan et al.[44] measured the fracture toughness of the BM, weld, and heat-affected zone (HAZ) of A106 Grade B pipe. The fracture toughness of the BM in air was 353–363 kJ m^{-2}. The fracture toughness in 102 atm hydrogen was 81–89 kJ m^{-2}. These relatively high values did not meet the plane strain fracture toughness condition. San Marchi and Somerday[45] reported that the fracture toughness reduced by 48%–60% after gaseous hydrogen charging in comparison to air. Nevertheless, the reduced value was still more than 100 MPa$\sqrt{m}$ for X70.

Alvarez et al.[46] measured the fracture toughness of structural steel in air and after hydrogen pre-charging for 21 h at 19.5 MPa. The fracture toughness of S355 in air and after hydrogen charging was 750 ± 20 and 306 ± 10 kJ m^{-2}, respectively. For H8, the fracture toughness was 450 ± 15 and 260 ± 13 kJ m^{-2}, respectively, in air and after hydrogen charging. Birenis et al.[47] studied commercially pure iron using compact tension specimens. Only crack blunting occurred without any stable crack propagation in air. In contrast, the crack propagated stably with less energy absorption in 0.7 and 90 MPa hydrogen, producing J_{IC} values between 50–60 kJ m^{-2}. Nguyen et al.[48] measured the fracture toughness of X70 in air, in 1% hydrogen blended with natural gas and in 100% hydrogen gas at 10 MPa as 205, 144, and 104 MPa$\sqrt{m}$, respectively.

Table 1. ASTM-valid values of fracture toughness from the literature. These values decrease with increasing gaseous hydrogen pressure.

Steel grade	Testing environment	Fracture toughness	References
X42, X52, X60, X70, X80	6.9 MPa H_2	95–111 MPa$\sqrt{m}$	[38]
A516 G70	Air	150 MPa$\sqrt{m}$	[41]
	3.5 MPa H_2	119 MPa$\sqrt{m}$	[41]
	6.9 MPa H_2	102 MPa$\sqrt{m}$	[41]
	20.7 MPa H_2	89 MPa$\sqrt{m}$	[41]
	34.5 MPa H_2	82 MPa$\sqrt{m}$	[41]
X42	Air	147 MPa$\sqrt{m}$	[43]
	4 MPa H_2	85 MPa$\sqrt{m}$	[43]
	6.5 MPa H_2	69 MPa$\sqrt{m}$	[43]
X70	Air	205 MPa$\sqrt{m}$	[48]
	10 MPa H_2	104 MPa$\sqrt{m}$	[48]
X65	Air	308 MPa$\sqrt{m}$	[88]

Decreasing fracture toughness with increasing hydrogen concentration has thus been established by the prior literature. **Table 1** summarizes the decrease of fracture toughness with increasing gaseous hydrogen pressure.

The next step is to establish the magnitude of the fracture toughness for Australian pipeline steels for the hydrogen concentrations possible for Australian gas transmission pipelines, which typically operate with pressures up to 15 MPa. Knowledge of the actual fracture toughness corresponding to the proposed hydrogen pressures in service allows the evaluation of the safe operating pressures and the critical crack sizes for Australian gas transmission pipelines transporting hydrogen. These are the major goals of this research. The research strategy is summarized in Section 1.4, and the research aims are summarized in Section 1.5.

1.2. Fracture and Fractography

The fracture and fractography of hydrogen-induced fracture of advanced high-strength steels (AHSSs) was reviewed by Atrens et al.[7] based on the prior studies.[49–51] AHSSs are similar to pipeline steels in that these steels also have a similarly low alloy content. These studies related to AHSSs electrochemically charged before and during linearly increasing stress tests (LISTs), which apply a slowly increasing stress to the specimen (under load control) until the specimen fractures at the maximum load. Hydrogen caused a decrease in the yield stress, attributed to solid solution softening by hydrogen. The decrease in yield strength was designated as hydrogen enhanced macroscopic ductility (HEMP). The fracture occurred at the ultimate tensile stress in the load-controlled LISTs at a stress somewhat lower than in air. The fracture mode was designated hydrogen-assisted microfracture (HAM). Ductile cup and cone fractures

(by microvoid coalescence [MVC]) occurred in air and for mild hydrogen-charging conditions and faster stressing rates. Higher hydrogen contents caused a more macroscopically brittle shear-type fracture at the ultimate tensile stress. There was no subcritical crack growth. Typically, hydrogen-influenced crack initiation at the surface was by mixed brittle intergranular/transgranular and MVC, and propagation was by ductile MVC. These findings of fractography (and the effect of hydrogen) were substantiated by the subsequent studies of Li et al.[52,53]

Zhang et al.[54] studied the tensile fracture and fractography of X65 pipeline steel subjected to tensile testing at a strain rate of $8 \times 10^{-5}\ s^{-1}$ soon after (within 3 min) electrochemical hydrogen charging at $45\ mA\ cm^{-2}$ for 24 h in 1) $0.5\ M\ H_2SO_4 + 5\ g\ L^{-1}$ thiourea (pH 1), 2) 3.5 wt% $NaCl + 5\ g\ L^{-1}$ thiourea (pH 6), and 3) 0.1 NaOH + $5\ g\ L^{-1}$ thiourea (pH 13). Thiourea is a hydrogen recombination poison and significantly increases the amount of hydrogen introduced into the specimen. The tensile ductility decreased in these charging solutions with decreasing solution pH which is expected to correlate with increasing hydrogen concentration. In solution (1) (pH13), the fracture was ductile, with dimples and microvoids being the main features, which would be assumed to be similar to the fractography in air. In solution (2) (pH 6), there was a mixture of brittle flat facets and ductile features (microvoids and dimples). In solution (3) (pH 1), there was only brittle quasi-cleavage.

Feaugas and co-workers[55–57] explored the impact of the form of hydrogen (trapped or diffusible) on the HE of a (quenched and tempered) martensitic Fe–0.3C alloy steel using a variety of smooth and notched specimens with various hydrogen-charging protocols. They found that the fracture of specimens containing only deeply trapped hydrogen was by ductile MVC similar to the fracture mode in air, indicating that trapped hydrogen facilitates ductile fracture. In contrast, diffusible hydrogen caused quasi-cleavage fracture. The fracture data was consistent with a local approach to fracture that fracture initiated under conditions such that there was a linear relationship between the hydrostatic stress (σ_m) and the von Mises equivalent plastic strain (ε_{peq}) as given in Equation (1).

$$\sigma_m = B + A\varepsilon_{peq} \tag{1}$$

where B and A are constants.

The popular mechanisms involving plasticity for hydrogen-induced subcritical crack advance include hydrogen-enhanced local plasticity (HELP) and adsorption-induced dislocation emission (AIDE). In addition, there is the HAM mechanism for hydrogen-induced fracture at the ultimate tensile stress, as discussed earlier. The HELP mechanism[58–64] proposes that hydrogen-facilitated dislocation motion causes the initiation and growth of microvoids ahead of the crack tip and that crack advance is caused by the linkage of these voids and the crack tip. The AIDE mechanism[65] proposes that hydrogen adsorbed at the crack tip facilitates dislocation emission, which advances the crack and that the enhanced dislocation activity ahead of the crack causes the formation of voids that link up with the crack tip causing crack advance. HAM was postulated by Atrens and co-workers[51,66] to explain the hydrogen-assisted fracture at the UTS of steels that propagated at speeds of 61–130 $m\ s^{-1}$, much faster than the ductile fracture velocity of 46 $m\ s^{-1}$ under the same condition of fracture under load control.

1.3. Cathodic Hydrogen Charging

Hydrogen-permeation testing was reviewed by Hoschke et al.[10] Cathodic hydrogen charging is equivalent to gaseous hydrogen charging at a particular hydrogen gas pressure, say 200 bar hydrogen, if the cathodic hydrogen charging produces an equilibrium hydrogen content the same as that produced in equilibrium by the gaseous hydrogen charging, provided that in both cases there is equilibrium between the hydrogen-charging condition and the hydrogen content in the steel.[67–70] The underlying principle is that hydrogen has no memory. The hydrogen dissolved inside the steel does not remember the source of the hydrogen. Using this approach, Liu et al.[70] evaluated the equivalent hydrogen fugacity versus overpotential for cathodic hydrogen charging in 0.1 M NaOH, as indicated in **Figure 1**, for 980 DP AHSS and compared these results with prior results for cathodic charging under similar conditions for the AHSS MS1500,[69] low interstitial steel,[67] and 3.5NiCrMoV steel.[68] The cathodic charging conditions can equivalently be characterized by the overpotential or by the charging current density, as in the research of Koren et al.[71] The fugacity of a gas is the pressure of that gas if the gas acted as an ideal gas. Figure 1 indicates that the hydrogen fugacity is essentially the same as the hydrogen pressure up to a hydrogen pressure of 100 atm.

Using this approach, Koren et al.[71] established for X65 the equivalency between gaseous hydrogen and electrochemical hydrogen charging in 3.5 wt% NaCl. Electrochemical hydrogen charging in 3.5 wt% NaCl at a current density of $9\ mA\ cm^{-2}$ was equivalent to pure gaseous hydrogen at 80 bar. This relationship may not be appropriate for slightly impure hydrogen as there is compelling experimental evidence that a trace of oxygen can inhibit gaseous HE.[11] Furthermore, the hydrogen concentration increased linearly with the square root of the hydrogen fugacity. The hydrogen concentration was 0.18 wt ppm for a hydrogen gas pressure of 200 bar.

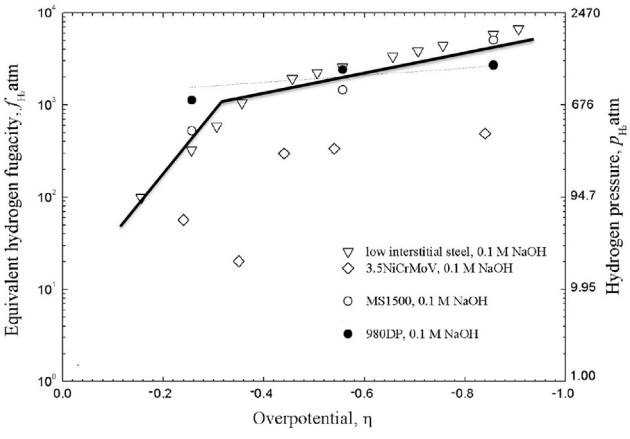

Figure 1. Hydrogen fugacity related to overpotential during cathodic hydrogen charging in 0.1 M NaOH solution for advanced high-strength steels (980DP and MS1500), low interstitial steel, and 3.5NiCrMoV steel. Reproduced with permission.[70] Copyright 2017, Wiley.

Research is underway at The University of Queensland to establish a relationship similar to that of Koren et al.[71] for cathodic charging of X65 in 0.1 M NaOH. Preliminary work suggested that cathodic charging at 9 mA cm^{-2} in 0.1 M NaOH is equivalent to exposure of X65 to pure gaseous hydrogen at 200 bar.

1.4. Research Strategy

This research aimed to measure the fracture toughness of the X65 pipeline steel, in the Dampier Bunbury natural gas transmission pipeline (DBNGP), corresponding to a hydrogen fugacity somewhat higher than the maximum service pressure for Australian gas transmission pipelines. The aim was to measure the fracture toughness corresponding to a longitudinal crack growing inward through the pipe wall in the radial direction. This is a critical situation for structural integrity. For the pipeline being considered, it is important to determine the fracture toughness of the steel used in this pipeline, because different X65 steels may have significantly different microstructures and different susceptibilities to HE. This preliminary research investigated the base material. Research is underway to investigate the weld material and the HAZ.

The typical gas-transmission pipe-wall thickness in Australia of 12.7 mm does not allow measurement of the fracture toughness with linear–elastic fracture mechanics according to the ASTM E1820 standard[12] (ASTM is the American Society for Testing of Materials). Instead, the fracture toughness was measured herein using elastic–plastic fracture mechanics according to the ASTM E1820 standard[12] using the J integral using fatigue pre-cracked single-edge-notch bend (SENB) specimens extracted from the pipeline wall of a representative pipe section. SENB specimens of two types were used as detailed in **Table 2**. Both conformed to ASTM E1820. Specimen type 2 was the largest specimen that could be extracted from the pipe wall.

The partial-unloading compliance method was used to determine the crack length, a, during the test. The J integral versus crack extension, Δa, was measured, and was plotted as the J–Δa curve. The resistance to stable crack extension was evaluated as the tearing modulus, as the slope of the J–Δa curve. Measurements were carried out for a uniformly hydrogen-charged specimen, which allows measurement of the fracture toughness and tearing modulus of the steel for that hydrogen concentration. Fractography was carried out to understand the fracture mechanism.

1.5. Research Aims

The research aims were as follows: 1) to measure the fracture toughness of DBNGP X65 pipeline steel for a hydrogen fugacity somewhat greater than in service and 2) to understand the mechanism by which hydrogen facilitates fracture.

2. Experimental Section

2.1. X65 Steel

The X65 steel was sourced from stockpile pipes so that the X65 steel was representative of the DBNGP. The chemical composition and mechanical properties were supplied by the pipe supplier. Specimen material was extracted for chemical analysis, metallography, tensile specimens for testing using the LIST,[49–51,72] and fracture toughness measurements using SENB specimens. The microstructure was examined for typical pipe cross sections in the radial and longitudinal directions. Typical specimens were mounted, ground, and polished using typical metallographic procedures, and etched in a nital 2% solution.

2.2. SENB Specimen

SENB specimens were extracted, as indicated in **Figure 2**, from an X65 pipeline with an outer diameter of 660 mm and wall thickness of 12.7 mm, for a crack extended in the longitudinal direction and growing in the radial direction. The ASTM designation was CR: the loading direction was circumferential (C), perpendicular to the crack plane, and the crack growth direction was radial (R) toward the inside of the pipe.

The two SENB specimen types followed the ASTM E1820 standard as illustrated in Figure 2a. The specimen dimensions are given in Table 2. Specimen type 1 was 8 mm wide (W) and 4 mm thick (B). Specimen type 2 was 10 mm wide (W) and 10 mm thick (B). Bolt-on knife edges were used to mount the crack-opening displacement (COD) gauge for specimen type 1. Integrated knife edges were used for specimen type 2. The specimens were designated as S.C.E.N., where S indicated specimen type 1 or specimen type 2, C indicated a plain-sided specimen (P) or a grooved specimen (G), E indicated environment as either air (A) or with hydrogen pre-charging and in situ charging at 9 mA cm^{-2} in 0.1 M NaOH (H9), and N indicated specimen number. The ASTM E1820 standard highly recommended side grooving for crack size estimation using the compliance method. The depth of the side groove, d, on each side of the specimen was 1 mm for specimen type 1 and 2 mm for specimen type 2.

SENB specimens were fatigue pre-cracked in three-point bending using load control. The applied initial maximum load was less than P_m given by

$$P_m = \frac{0.5 B b_0^2 \sigma_y}{S} \tag{2}$$

Table 2. SENB specimen dimensions.

Specimen type	Specimen thickness, B [mm]	Width, W [mm]	Support span, S [mm]	Length, l [mm]	Notch depth [mm]	Fatigue pre-crack length [mm]	Total crack length, a_0 [mm]	b_0, ($W-a_0$) [mm]	d [mm]
1	4	8	32	48	2.50	1.50	4.5	3.5	1
2	10	10	40	60	3.00	2.00	5.0	5.0	2

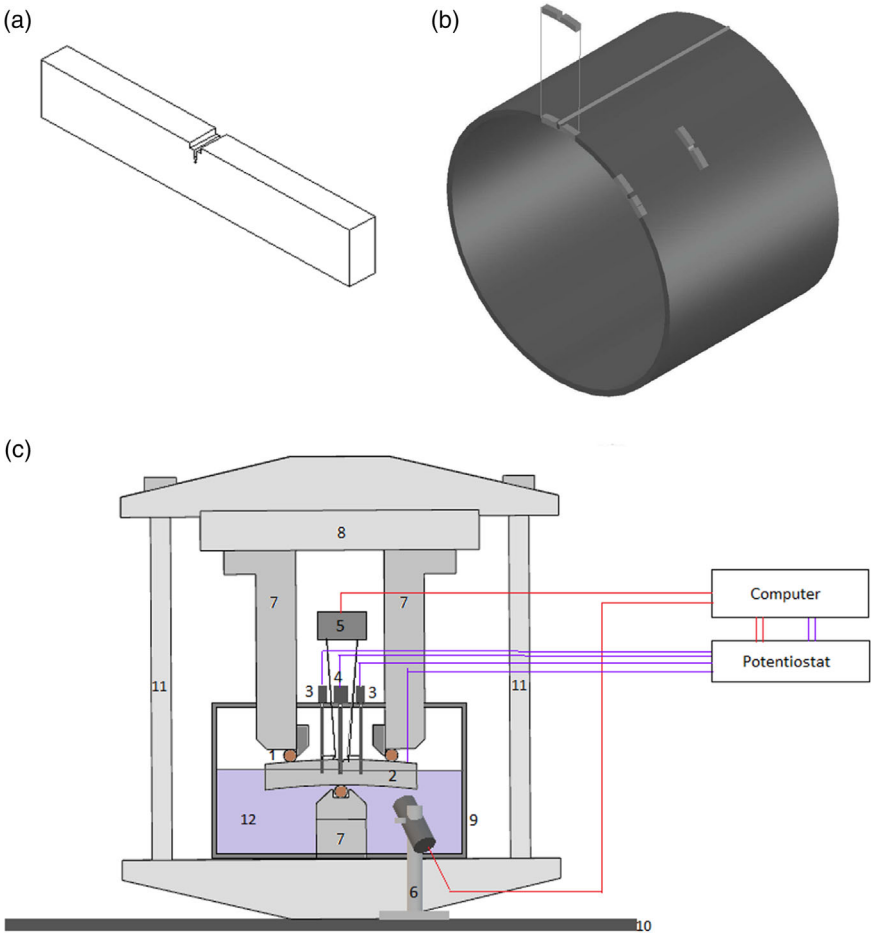

Figure 2. a) Schematic of an SENB specimen. b) Extraction of the SENB specimen from the steel pipe segment to evaluate the fracture toughness for a crack extended in the longitudinal direction growing in the radial direction. c) Schematic of the three-point bend apparatus for the measurement of the fracture toughness (measured as the *J* integral) using an SENB specimen using the partial unloading compliance method to determine the crack length. Hydrogen was charged into the specimen using cathodic hydrogen charging. The apparatus involved the following components: 1) alumina ceramic rollers, 2) SENB test specimen, 3) counter electrode, 4) reference electrode, 5) COD gauge, 6) digital microscope, 7) three-point bend fixtures, 8) T-slot, 9) electrolytic cell, 10) metal plate, 11) alignment bar, and 12) electrolytic solution. The apparatus was designed for a specimen as depicted in Figure 2a, or a curved specimen with the full-wall thickness of the gas-transmission pipeline as indicated by the specimen in the figure.

where $\sigma_y = (\sigma_{YS} + \sigma_{UTS})/2$; σ_{YS} is the 0.2% offset yield strength, σ_{UTS} is the ultimate tensile strength, S is the span length, B is the specimen thickness, and b_0 is the uncracked ligament length given by $b_0 = W–a_0$, where W is the specimen width and a_0 is the initial crack length. The maximum frequency for fatigue pre-cracking was 35 Hz. The ratio (R) between minimum and maximum force was 0.1. When the crack did not start after 10^5 cycles, the load was increased incrementally until a fatigue crack started. Crack growth was monitored using a digital camera. When the fatigue crack reached 50% of the desired pre-crack length, the load was reduced to P_m for the final 50% of the fatigue pre-crack.

2.3. Three-Point Bend Apparatus

A three-point bend apparatus was produced to measure the fracture toughness of the SENB specimens in air and with in situ cathodic hydrogen charging with the specimen the cathode as presented in Figure 2. Hydrogen was introduced into the specimen before and during the fracture toughness test. During the cathodic hydrogen pre-charging, the crack tip was below the surface of the solution, and a load was applied equal to 20% P_m. The cathodic pre-charging time was sufficient to ensure a constant hydrogen content in an unstressed specimen. For the stressed specimen used herein, the hydrogen content at the crack tip was raised by the triaxial stress at the crack tip. The hydrogen ingress was essentially through the specimen sides and bottom of the specimen, as it was well known that the potential decreases rapidly in a crack-like feature. The cathodic hydrogen charging continued during the entire fracture-mechanics test. The aim was to use electrochemical hydrogen charging to produce a hydrogen concentration somewhat greater than that produced by the maximum service gas pressures of 15 MPa (150 bar).

Ceramic rollers applied load and electrically isolated the specimen. The upper part of the apparatus accommodated the COD

gauge. The crack growth was monitored on both sides of the specimen during the test using two digital microscopes. The electrochemical charging used a three-electrode cell with 1) the SENB specimen as the working electrode, 2) a reference electrode and 3) a graphite counter electrode. The specimen was electrochemically charged in 0.1 M NaOH at 9 mA cm^{-2} for a time sufficient to ensure a uniform hydrogen concentration throughout the specimen section: 48 h for the 4×8 mm section specimens and 96 h for the 10×10 mm section specimens. The required time was modeled based on hydrogen diffusion and the hydrogen diffusion coefficient of 6.2×10^{-7} cm^2 s^{-1}, which was measured separately[25,73]

After the fracture toughness test, each SENB specimen was cooled down in liquid nitrogen and broken into two parts. Fractographic examination was carried out using a JEOL JSM 7800 F field emission SEM of three typical specimens: 1) 1S.A.1 side-grooved type 1 specimen tested in air, specimen number 1; 2) 1S.H9.1 side-grooved type 1 specimen tested with hydrogen charging, specimen number 1; and 3) 2S.H9.1 side-grooved type 2 specimen tested with hydrogen charging, specimen number 1. The fractography was carried out without any surface coating.

2.4. Fracture Toughness Test

The three-point bend test followed the ASTM E1820 standard. The fatigue pre-cracked SENB specimen was mounted onto the three-point bend apparatus in a servo hydraulic testing machine and loaded under displacement control. A COD gauge recorded the *COD*. The elastic compliance technique evaluated the crack length from the partial unloading/reloading sequence. The measured crack length was verified by optical measurements of the initial and final crack length after the fracture toughness test. The original crack length was first measured by loading and unloading the specimen three times at a constant crosshead speed such that the maximum force P_m was reached between 0.1 and 3.0 min. The unloading/reloading sequence had a force range of 0.5 P_m to P_m. Thereafter, the specimen was loaded, and the unloading and reloading of the sample were continued until sufficient crack extension was achieved. The range of unloading was between 10% and 30% of P_{m}. The crack size, a_i, was evaluated following the ASTM E1820 standard using

$$\frac{a_i}{W} = [0.999748 - 3.9504\,u + 2.9821\,u^2 - 3.21408\,u^3 + 51.51564\,u^4 - 113.031\,u^5] \tag{3}$$

where

$$u = \frac{1}{\left[\frac{B_e W E C_i}{S/4}\right]^{1/2} + 1} \tag{4}$$

where E is the elastic modulus and C_i is the elastic compliance. The partial unloading of the specimen during the specimen loading enabled the evaluation of the slope of the unloading part of the force–*COD* curve. The compliance is the inverse of the slope and is given by

$$C_i = \frac{\Delta V_{\mathrm{m}}}{\Delta P} \tag{5}$$

where ΔV_m is the change in the *COD* and ΔP is the change in load, the effective thickness $B_{\mathrm{e}} = B - (B - B_{\mathrm{N}})^2/B$ and B_{N} is the net specimen thickness after side grooving. For a plain-sided specimen, $B_{\mathrm{N}} = B$, since the specimen does not have any side grooves.

The length of the crack evaluated by the ASTM compliance method using Equation (3) was compared with the length of the crack measured optically on the specimen after the fracture toughness test for 1) the initial crack length after fatigue pre-cracking and 2) the final crack length after the fracture toughness test. The physical crack length (measured optically), L_{o}, of the initial and final crack was measured as specified in ASTM E1820 at nine equally spaced points along the crack front curvature according to Equation (6).

$$L_{\mathrm{o}} = \left[\left(\frac{a_1 + a_9}{2}\right) + \sum_{i=2}^{8} a_i\right] \Big/ 8 \tag{6}$$

where a_1 and a_9 are the crack length measured at a distance 0.05 W from the root of the side groove and a_i represent the other seven measurements of the crack length.

The J integral was evaluated at each unloading for the force versus crack-mouth-opening displacement (*CMOD*) curve. The J integral for every corresponding crack extension was plotted versus Δa_i. A construction line was plotted according to Equation (7) (according to the ASTM E1820 standard) or Equation (8) (considering the effect of strain hardening on the X65 pipeline steel sample).

$$J = 2\sigma_{\gamma}\Delta a \tag{7}$$

or

$$J = 4.23\sigma_{\gamma}\Delta a \tag{8}$$

Four parallel lines were drawn at 0.15, 0.2, 0.5, and 1.5 on the X axis representing Δa_i. The data points that fell between the lines at 0.15 and 1.50 were the qualified data used for determining J_{Ic}. At least one data point from the qualified data should lie on both sides of the line at 0.5. The coefficients of the power law equation between J and Δa were determined using the qualified data by fitting the data to the following equation:

$$J = C_1\left(\frac{\Delta a}{k}\right)^{C_2} \tag{9}$$

Using the qualified data, a power least-square-regression analysis was carried out using the power law linearized in the following form:

$$\ln(J) = \ln(C_1) + C_2 \ln\left(\frac{\Delta a}{k}\right) \tag{10}$$

where $k = 1.0$ mm. The intersection between the J–Δa_i curve and the 0.2 construction line represented the provisional J_{Q} and Δa_{Q}. The provisional J_{Q} qualifies as J_{Ic} (or J_{IH}) if the following conditions are met.

$$\text{Thickness, } B > \frac{10J_Q}{\sigma_y} \tag{11}$$

$$\text{Initial ligament, } b_0 > \frac{10J_Q}{\sigma_y} \tag{12}$$

K_{JIc} was evaluated using the following equation:

$$K_{JIc} = \sqrt{E' J_{Ic}} \tag{13}$$

where

$$E' = \frac{E}{(1-\nu^2)} \tag{14}$$

2.5. Construction Line

Li et al.[74] indicated that the equation used for the construction line or blunting line is

$$J = 2m\sigma_y \Delta a \tag{15}$$

where σ_y is the yield strength as defined for Equation (2) and m is a constant ($1 \leq m \leq 2.6$). The ASTM E1820 standard used $2m = 2$, and the construction line was as shown in Equation (7). However, m depended on the material properties and could be evaluated using Equation (16):[75]

$$2m = \left(\frac{E}{R_m}\right)\left(\frac{1}{0.4d_n^*}\right) \tag{16}$$

where d_n^* is the blunting line coefficient, R_m is the ultimate strength, E is the Young's modulus, and d_n^* can be evaluated using Equation (17)[75]

$$d_n^* = \left(\frac{\sigma_0}{E}\right)^{n-1}\left(0.787 + 1.554n - 2.450n^2 + 16.952n^3 - 38.206n^4 + 33.130n^5\right) \tag{17}$$

Alternatively, d_n^* can be determined graphically using Figure A1 in Appendix. The hardening exponent (n) could be evaluated according to Equation (18) as proposed in the European Structural Integrity Society (ESIS) standard P2-92:[75]

$$\frac{\sigma_{YS}}{\sigma_{UTS}} = \frac{1}{1+\varepsilon_{p0.2}}\left[\frac{2.718\ln(1+\varepsilon_{p0.2})}{n}\right]^n \tag{18}$$

where σ_{YS} is the yield strength, σ_{UTS} is the ultimate tensile strength and

$$\varepsilon_{p0.2} = \frac{\sigma_{YS}}{E} + 0.002 \tag{19}$$

Alternatively, the hardening exponent (n) could be determined graphically using Figure A2 in the Appendix. The calculated m is inserted in Equation (15) for plotting the construction line.

Landes[76] recommended 3.75 for the value of $2m$ in the blunting line equation (Equation (15)), so that the blunting line equation became as in the ISO 12135 (2002) standard:

Table 3. Coefficient of the construction line.

σ_{YS} [MPa]	σ_{UTS} [MPa]	E [GPa]	$\varepsilon_{p0.2}$	n	d_n^*	$2m$
510	590	210	0.00443	0.85	210	4.23

$$J = 3.75\sigma_{UTS}\Delta a \tag{20}$$

For the X65 used in this research, the coefficient of the construction line was 4.23 as shown in **Table 3**. Thus, the equation for the construction line was as given in Equation (8).

Similar construction lines have been used previously. Joseph et al.[77] studied the fracture toughness of X65 pipeline steel in fuel-grade ethanol. The slope of the construction line was evaluated using the mechanical properties of X65 as $5\sigma_0$ where σ_0 was the flow stress. The measured fracture toughness (J_Q) was 536 kJ m^{-2}. Gajdos et al.[78] measured the fracture toughness of the pipeline steel L450MB. The slope of the construction was $4\sigma_y$ where σ_y was the flow stress (the average value of yield strength and ultimate tensile strength). The measured J_Q was 495 kJ m^{-2}. Gao et al.[79] also calculated the slope of the construction line while measuring the fracture toughness of material with small strain-hardening exponents, such as structural steel Weldox700, G350, and G250.

3. Results

3.1. X65 Steel Characterization

The chemical composition of the X65, as presented in **Table 4**, indicated a low-carbon steel with some alloying of Si and Mn and the presence of some microalloying (Nb). The microstructure in the radial and longitudinal directions is presented in **Figure 3**. The microstructure indicated a typical banded ferrite and pearlite microstructure, elongated in the longitudinal direction, which corresponded to the direction of rolling of the steel plate. The light phase was ferrite. The darker microconstituent was pearlite, which was not resolved at this magnification. This microstructure was as expected for this type of steel in Australian gas transmission pipelines[80–84] although there are also other X65 steel grades that have microstructures containing bainite or acicular ferrite. The tensile properties of the pipeline steel X65 are presented in **Table 5**.

3.2. Force *CMOD* Curves

The force versus *CMOD* curves for the three-point bend tests using the single-edge-notched specimen type 1 are presented in **Figure 4**. After each load application, the load was decreased to measure the crack length from the compliance. The maximum force for the uncharged side-grooved specimen in air (1S.A.1) was 1274 N, corresponding to a *CMOD* of 0.998 mm. Specimen 1S.H9.2 (side grooved) with in situ cathodic hydrogen charging at 9 mA cm^{-2} reached the same maximum force at the much lower *CMOD* of 0.600 mm. In contrast, the maximum force reached by specimen 1S.H9.1 (side grooved) with in situ cathodic hydrogen charging was 974 N at a *CMOD* of

Table 4. Chemical composition of the X65 pipeline steel, wt%.

C	Si	Mn	P	S	Al	Cr	Mo	Ni	Co	Cu	Nb	Ti	V
0.12	0.26	1.51	0.02	0.006	0.033	0.02	0.01	0.01	0.003	0.01	0.04	0.001	0.005

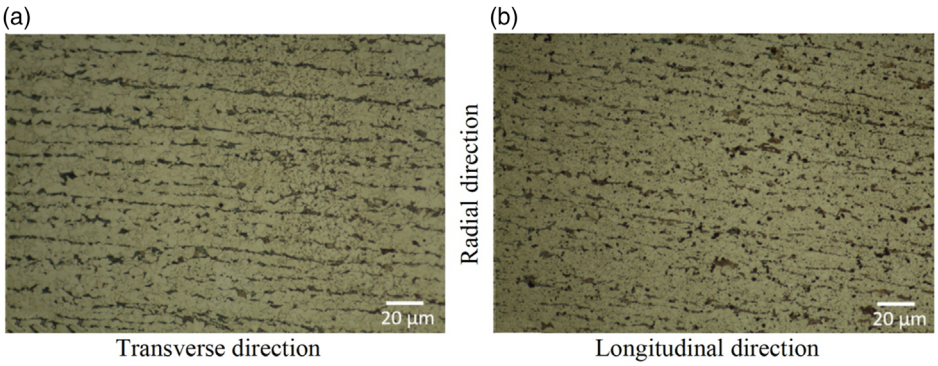

Figure 3. Microstructure of the X65 in a) the radial–transverse plane and b) the radial–longitudinal plane.

Table 5. Tensile properties of the X65 pipeline steel.

Yield strength, σ_y [MPa]	Tensile strength, σ_{UTS} [MPa]	Young's modulus, E [GPa]	Poisson's ratio
510 ± 5	590 ± 5	210	0.3

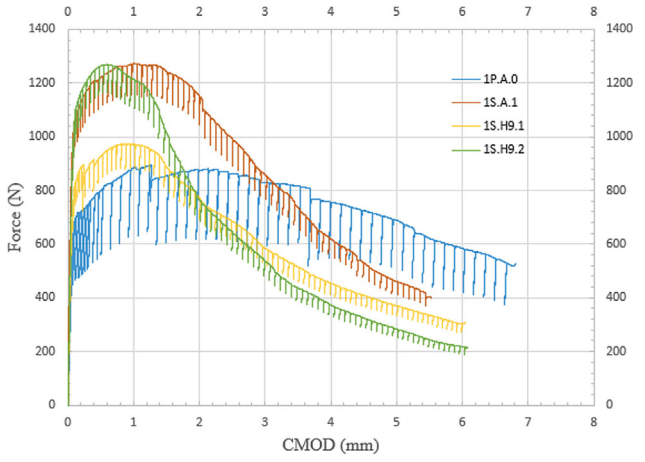

Figure 4. Force versus *CMOD* for the following specimens of type 1: 1P.A.0 (plain specimen tested in air); 1S.A.1 (side-grooved specimen tested in air); 1S.H9.1 (side-grooved specimen tested with hydrogen charging); and 1S.H9.2 (side-grooved specimen tested with hydrogen charging).

0.870 mm. The maximum force for the side-grooved specimens was significantly higher than for the plain-sided specimen in air.

The force–*CMOD* curves for the three-point bend test using the single-edge-notched specimen type 2 are presented in **Figure 5**. The maximum force for the uncharged side grooved

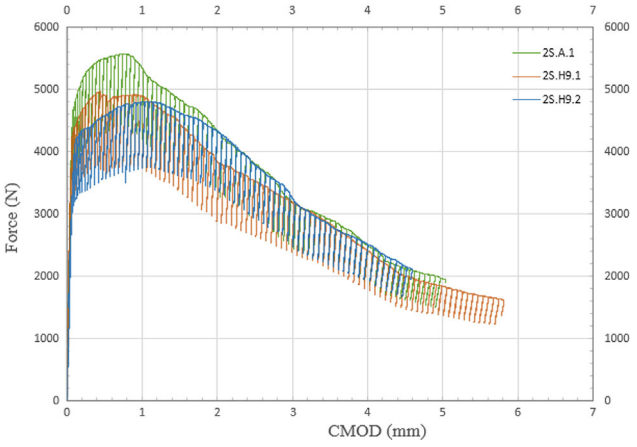

Figure 5. Force–*CMOD* curve for the following specimens of type 2: 2S.A.1 (side-grooved specimen tested in air); 2S.H9.1 (side-grooved specimen tested with hydrogen charging); 2S.H9.2 (side-grooved specimen tested with hydrogen charging).

specimen in air (2S.A.1) was 5570 N corresponding to a *CMOD* of 0.75 mm. Specimen 2S.H9.1 with in situ cathodic hydrogen charging of 9 mA cm^{-2} reached a maximum force of 4970 N at the *CMOD* of 0.44 mm. The maximum force reached by specimen 2S.H9.2 with in situ cathodic hydrogen charging was 4800 N at a *CMOD* of 1.05 mm.

The ASTM E1820 standard defines "stable crack extension" as a displacement-controlled crack extension, such that the extension stops when the applied displacement is held constant. The standard defines "unstable crack extension" as an abrupt crack extension in a specimen under displacement control. An unstable crack extension is designated as a "fracture instability". A single-point value of fracture toughness can be evaluated corresponding to the instability. Such unstable crack extensions

Table 6. Conditions for unstable crack extension for Figure 4 and 5 and associated parameters.

Specimen designation	B [mm]	b_0 [mm]	σ_y [MPa]	*CMOD* at instability [mm]	Size significant	J_{QC} [kJ m^{-2}]	K_{JQ} [MPa$\sqrt{m}$]	$\frac{100J_{Qc}}{\sigma_y}$	B, $b_0 > \frac{100J_{Qc}}{\sigma_y}$
1P.A.0	4	–	510	1.2	Yes	222	–	–	–
	4	–	510	3.8	–	–	–	–	–
	4	–	510	5.2	–	–	–	–	–
1S.A.1	4	3.42	510	2.1	–	–	–	–	–
1S.H9.1	4	3.07	510	0.21	Yes	37	92	7	No
	4	3.07	510	0.33	Yes	65	122	13	No
	4	3.07	510	0.46	Yes	97	150	19	No
2S.H9.1	10	4.51	510	0.43	Yes	132	174	26	No
	10	4.51	510	0.47	Yes	148	184	29	No
	10	4.51	510	0.52	Yes	172	199	34	No

were indicated by the force versus *CMOD* curve in Figure 4 and 5 at the *CMOD* values listed in **Table 6**.

The ASTM E1820 standard annex A4 provides methods for the evaluation of an "instability" or "pop-in". Annex A4 uses the designation "pop-in" throughout; however, the section heading indicates applicability to an instability. The methods of A4 have been used to assess the size significance of each fracture instability in Table 8 as "Yes" or "No".

The ASTM E1820 standard annex A4 also indicates that a fracture instability is only evaluated if the instability is followed by a load increase. For specimen 1P.A.0, this rule indicated that a fracture toughness value could be evaluated for the *CMOD* value of 1.2 mm but not for 3.8 and 5.2 mm. In addition, for specimen 1P.A.0, the measured crack extension was under-predicted because of the plastic deformation, and absence of side grooves. In addition, it was not appropriate to evaluate J_{QC} for 1S.A.1 because the instability occurred when the corresponding crack length was more than $0.2\,\text{mm} + J_{QC}/2\sigma_y$. Thus, the intersection between the J–Δa curve and the 0.2 mm offset line was evaluated as J_Q for specimen 1S.A.1.

In contrast, Figure 4 indicates that fracture instabilities for 1S.H9.1 occurred before the crack length reached $0.2\,\text{mm} + J_{QC}/2\sigma_y$ at *CMOD* values of 0.21, 0.33, and 0.46 mm, so that fracture toughness values could be evaluated corresponding to these values.

Similarly, for 2S.H9.1, fracture instabilities occurred before the crack length reached $0.2\,\text{mm} + J_{QC}/2\sigma_y$ at *CMOD* values of 0.43, 0.47, and 0.52 mm, so that the corresponding fracture toughness values could be evaluated. The ASTM E1820 annex 6 indicates that the fracture instability toughness is evaluated at the final point, instability, and is designated J_{QC}. Consequently, the fracture toughness for 1S.H9.1 and 2S.H9.1 was evaluated at the 0.46 mm *CMOD* and 0.52 mm *CMOD*, respectively.

3.3. Crack Length

The elastic compliance for each unloading was evaluated using Equation (5), was normalized using Equation (4), and was used to evaluate the crack length using Equation (3). This measured crack length was compared with the initial and final crack length on the specimen measured optically after the fracture-mechanics test. **Figure 6** illustrates the optical measurements of the crack length. **Table 7** provides the numerical values. The difference

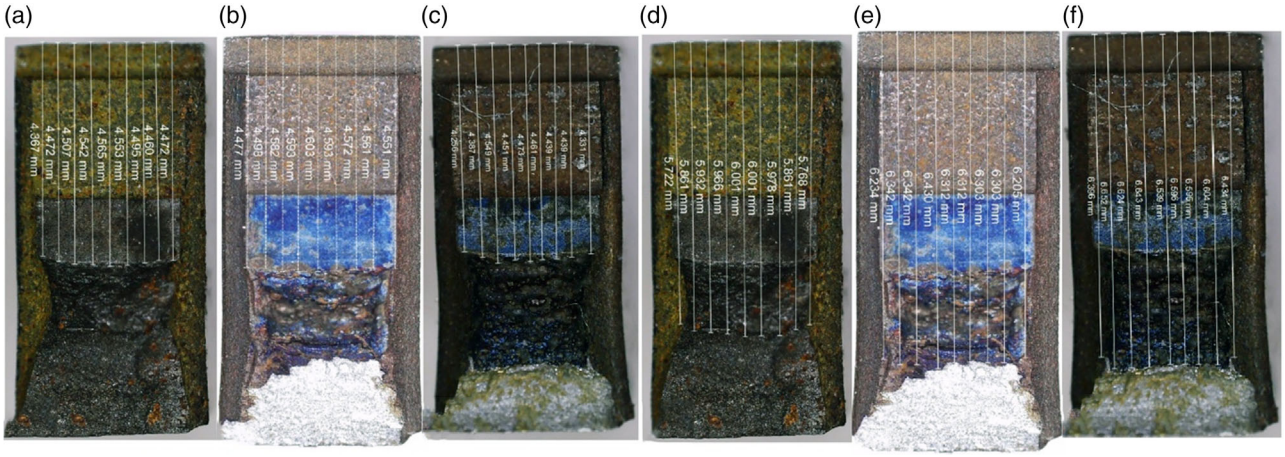

Figure 6. Initial crack length measurements for specimens tested in a) air (1S.A.1), b) at 9 mA cm^{-2} (1S.H9.1), and c) at 9 mA cm^{-2} (1S.H9.2). Final crack length measurements for specimens tested in d) air (1S.A.1), e) at 9 mA cm^{-2} (1S.H9.1), and f) at 9 mA cm^{-2} (1S.H9.2).

Table 7. Comparison of crack length as determined from the compliance and by optical measurement for specimen type 1.

Test condition	Specimen	Compliance	Optical	Difference	Within limit
		Initial crack length [mm]			
In air	1S.A.1	4.57	4.50	0.07	Yes
9 mA cm^{-2}	1S.H9.1	4.93	4.56	0.37	Yes
9 mA cm^{-2}	1S.H9.2	4.64	4.43	0.21	Yes
		Final crack length [mm]			
In air	1S.A.1	6.07	5.97	0.10	Yes
9 mA cm^{-2}	1S.H9.1	6.45	6.38	0.07	Yes
9 mA cm^{-2}	1S.H9.2	6.50	6.58	0.08	Yes

between the initial length measured optically and by the elastic compliance method should not exceed 0.5 mm or 0.01 W whichever is larger. In this work, $W = 8$ and 0.01 W was 0.08 mm. Thus, the difference should not be more than 0.5 mm. The difference was within the allowable limit for the initial and final crack length, as documented in Table 7.

Table 8 provides the crack length comparison for specimen type 2. For the initial crack length, the difference should be less than 0.5 mm. The measured initial crack lengths did not meet the requirement as shown in Table 8. The final crack length measurements were also compared in Table 8. The maximum allowable difference between these two should be less than $0.03b_0$ where b_0 is the initial ligament of the specimen. None of the measured crack lengths met the requirement except specimen 2S.H9.1 tested with in situ cathodic hydrogen charging. In all cases, the crack length measured using the compliance method was longer than the actual crack length measured optically.

3.4. Fracture Toughness, Type 1 Specimens, $2m = 2$

The J–Δa curves for specimen type 1 are presented in **Figure 7**, in which the construction line is given by Equation (7), using $2m = 2$. Parallel lines were drawn to give the 0.15 mm exclusion line, the 0.2 mm offset line, the 0.5 mm offset line, and the 1.5 mm exclusion line. The data for the plain-sided specimen

Table 8. Crack length comparison for specimen type 2.

Test condition	Specimen	Compliance	Optical	Difference	Within limit
		Initial crack length [mm]			
In air	2S.A.1	5.25	4.71	0.54	No
9 mA cm^{-2}	2S.H9.1	5.49	4.73	0.77	No
9 mA cm^{-2}	2S.H9.2	5.71	5.16	0.55	No
		Final crack length [mm]			
In air	2S.A.1	7.91	7.60	0.31	No
9 mA cm^{-2}	2S.H9.1	7.92	7.81	0.11	Yes
9 mA cm^{-2}	2S.H9.2	7.89	7.74	0.14	No

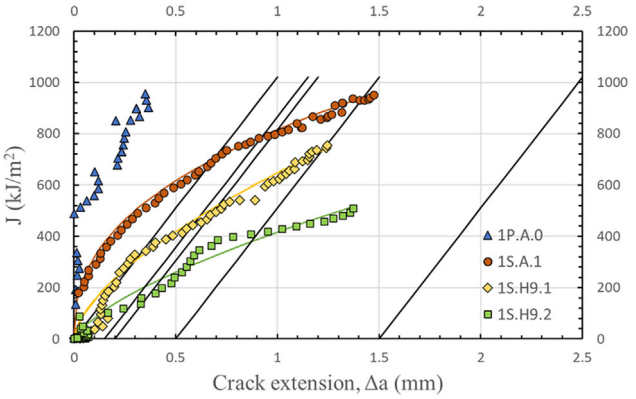

Figure 7. J–Δa curve (and construction lines using $J = 2\sigma_y \Delta a$) for the following type 1 specimens: 1P.A.0 (plain specimen tested in air); 1S.A.1 (side-grooved specimen tested in air); 1S.H9.1 (side-grooved specimen tested with hydrogen charging); and 1S.H9.2 (side-grooved specimen tested with hydrogen charging).

(1P.A.1) did not intersect with the construction lines, so no estimate of the fracture toughness could be evaluated for this specimen.

For the side-grooved specimens, the minimum data point requirement was checked. All the monotonically increasing data points between the 0.15 mm exclusion line and the 1.5 mm offset line were used for evaluating the coefficients of the power law regression relationship between J and Δa, which was linearized using Equation (10). However, the data points for specimen 1S.A.1 tested in air and specimen 1S.H9.1 tested with hydrogen did not fall below the maximum J_{max} limit ($b_0\sigma_y/10$ or $B\sigma_y/10$). In contrast, the data points used for constructing the curve fit for specimen 1S.H9.2 were nearly within the J_{max} limit. The intersection between the power regression line and the 0.2 mm offset line gave the provisional fracture toughness (J_Q) at 0.2 mm crack extension, except for 1S.H9.1, which was evaluated corresponding to ≈0.2 mm *CMOD* as justified in Section 3.2. The provisional J_Q values are presented in **Table 9**.

Provisional J_Q value qualifies as a valid J_{1C} value if the conditions of Equation (11) and (12) are satisfied. **Table 10** summarizes the validity check. The provisional J_Q for specimen 1S.A.1 tested in air and the hydrogen-charged specimen 1S.H9.1 did not meet the conditions for a valid J_{1C}. When the measured fracture toughness does not meet the criteria for a valid J_{1C}, the measured value depends on the specimen size. The provisional J_Q for the hydrogen-charged specimen 1S.H9.2 did meet the conditions for a valid J_{1C}.

Table 9. Provisional J_Q values for type 1 specimens using the construction line $J = 2\sigma_y \Delta a$.

Test condition	Specimen designation	Initial crack size, a_{oq} [mm]	Final crack size, a_p [mm]	Crack extension [mm]	J_Q [kJ m^{-2}]
In air	1S.A.1	4.579	6.076	1.497	808
9 mA cm^{-2}	1S.H9.1	4.930	6.450	1.520	97
9 mA cm^{-2}	1S.H9.2	4.642	6.509	1.866	170

Table 10. Criteria check for valid J_{1C} or J_{1H} for type 1 specimens using the construction line $J = 2\sigma_\gamma \Delta a$.

Test condition	Specimen designation	B [mm]	W [mm]	a_{oq} [mm]	b_0 [mm]	σ_γ [MPa]	$J_{Q0.2}$ [kJ m^{-2}]	$\frac{10J_Q}{\sigma_\gamma}$	B, $b_0 > \frac{10J_Q}{\sigma_\gamma}$
In air	1S.A.1	4	8	4.58	3.42	510	808	15.84	No
9 mA cm^{-2}	1S.H9.1	4	8	4.93	3.07	510	97		Yes
9 mA cm^{-2}	1S.H9.2	4	8	4.65	3.35	510	170	3.33	Yes

3.5. Fracture Toughness, Type 1 Specimens, $2m = 4.23$

The fracture toughness was evaluated using the J–Δa curves as in **Figure 8** for type 1 specimens, using the construction line $J = 4.23\sigma_\gamma \Delta a$, in which $2m = 4.23$. The numerical factor was calculated as in Table 3 using the procedure recommended by the ESIS in the fracture-mechanics testing standard ESIS P2-92. An evaluation was possible for the side-grooved specimens, but no evaluation was possible for the plain-sided specimen. The intersection between the power regression line and the 0.2 mm offset line gave the provisional fracture toughness (J_Q) at 0.2 mm crack extension. The measured J_Q are presented in **Table 11**.

The determined provisional J_Q qualifies as a valid J_{1C} if the conditions of Equation (11) and (12) are met. The determined provisional J_Q for the uncharged specimens 1S.A.1 did not meet the conditions for a valid J_{1C}, as indicated in **Table 12**. The provisional J_Q for specimen 1S.H9.2 at 9 mA cm^{-2} did meet the conditions for a valid J_{1C}. Furthermore, Figure 8 indicates that, because of the steeper construction lines, the data points used for constructing the curve fit for specimen 1S.H9.2 were essentially within the J_{max} limit.

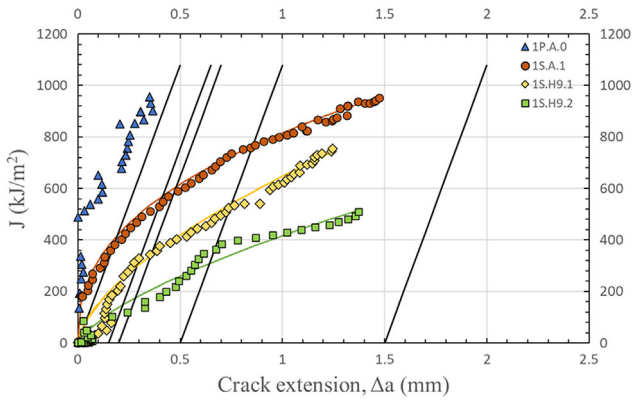

Figure 8. J–Δa curves (using the construction line $J = 4.23\sigma_\gamma \Delta a$) for the following type 1 specimens: 1P.A.0 (plain-sided specimen tested in air); 1S.A.1 (side-grooved specimen tested in air); 1S.H9.1 (side-grooved specimen tested with hydrogen charging); and 1S.H9.2 (side-grooved specimen tested with hydrogen charging).

Table 11. Fracture toughness evaluations for specimen type 1 using the construction line $J = 4.23\sigma_\gamma \Delta a$.

Test condition	Specimen designation	Initial crack size, a_{oq} [mm]	Final crack size, a_p [mm]	Crack extension [mm]	J_Q [kJ m^{-2}]
In air (side grooved)	1S.A.1	4.579	6.076	1.497	590
9 mA cm^{-2}	1S.H9.1	4.926	6.449	1.524	97[a)]
9 mA cm^{-2}	1S.H9.2	4.642	6.508	1.866	155

[a)] Designated as J_{QC}.

The energy for stable crack growth increased with crack length, as indicated by the positive slopes of the J–Δa curves in Figure 8 in each case, including the two specimens containing hydrogen. Quantification is possible using the tearing modulus, which is the slope of the J–Δa curve for crack lengths somewhat greater than those used to determine the fracture toughness. Figure 8 indicates that the tearing modulus for each of the two specimens containing hydrogen was less than that of the specimen tested in air. This indicates that the incremental energy for stable crack growth with hydrogen was lower than for the tests in air. Nevertheless, the energy for stable crack growth with hydrogen did increase with increasing crack length.

The fracture toughness values measured in this work were consistent with literature values. X65 has high toughness.For example, Joseph[85] measured fracture toughness values for X65 as J integral in air and the test environments of E20 and E20 + 32 mg L^{-1} NaCl as 536, 399, and 488 kJ m^{-2}, respectively (converted to a stress intensity factor (K) as 351, 303, and 336 MPa$\sqrt{m}$). The measured fracture toughness did not qualify as J_{1c} and was not size independent. The values can only be compared with a specimen of a similar size. Similarly, Hashemi et al.[86] could not measure a valid J_{1C} due to the limitation of the pipe thickness. The experimentally measured value was 308 MPa$\sqrt{m}$. Lee et al.[87] also measured the fracture toughness of X65 pipeline steel that also did not meet the criteria for plane-strain fracture toughness (J_{1C}) due to size limitations. The fracture toughness of the BM was 300, 363, and 315 MPa$\sqrt{m}$ for the upper, middle, and lower regions for a circumferential crack. Torshizian et al.[88] measured valid J_{1C} values for X65 for the BM and the weld zone. The measured fracture toughness of the BM and welded zone was 308 and 177 MPa$\sqrt{m}$ (corresponding to a J-integral value of 136 kJ m^{-2}).

3.6. Fracture Toughness, Type 2 Specimens, $2m = 4.23$

The J–Δa curve is presented in **Figure 9**. The data for specimen type 2 were analyzed only using the construction line $J = 4.23\sigma_\gamma \Delta a$, because this provided a smaller value of fracture toughness and therefore provided a more conservative structural integrity analysis. The monotonically increasing data between the 0.15 mm construction line and the 1.5 mm exclusion line were

Table 12. Criteria check for valid J_{1C} or J_{1H} for type 1 specimens using the construction line $J = 4.23\sigma_y\Delta a$.

Test condition	Specimen	B [mm]	W [mm]	a_{oq} [mm]	b_0 [mm]	σ_y [MPa]	J_Q [kJ m^{-2}]	K_Q [MPa$\sqrt{m}$]	$\frac{10J_Q}{\sigma_y}$	B, $b_0 > \frac{10J_Q}{\sigma_y}$
In air	1S.A.1	4	8	4.58	3.42	510	590	369	15.84	No
9 mA cm^{-2}	1S.H9.1	4	8	4.93	3.07	510	97[a)]	150	–	–
9 mA cm^{-2}	1S.H9.2	4	8	4.65	3.35	510	155	189	3.33	Yes

[a)]Designated as J_{QC}; there are difference size requirements.

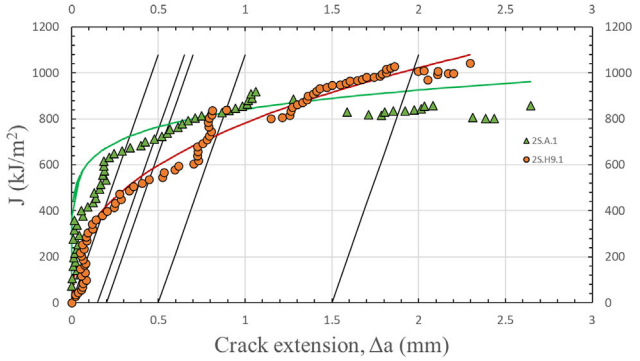

Figure 9. J–Δa curve (and construction lines using the construction line $J = 4.23\sigma_y\Delta a$) for the following specimens of type 2: 2S.A.1 (side-grooved specimen tested in air) and 2S.H9.1 (side-grooved specimen tested with hydrogen charging), as indicated in Table 13.

used for fitting the power law regression line. However, the data points did not fall within the area enclosed by the maximum J_{max}. There was significant apparent negative crack growth for specimen 2S.H9.2 so this data could not be used further. The measured J_Q values are shown in **Table 13**. The determined provisional J_Q for both the charged and uncharged specimens did not meet the conditions for a valid J_{1C}, as indicated in **Table 14**.

Table 13. Provisional J_Q values for type 2 specimens.

Test condition	Specimen designation	Initial crack size, a_{oq} [mm]	Final crack size, a_p [mm]	Final crack extension [mm]	J_Q [kJ m^{-2}]
In air (side grooved)	2S.A.1	5.25	7.91	2.66	778
9 mA cm^{-2}	2S.H9.1	5.49	7.92	2.42	172[a)]

[a)]Designated as J_{QC}.

Table 14. Criteria check for valid J_{1C} for type 2 specimens.

Test condition	Specimen designation	B [mm]	W [mm]	a_{oq} [mm]	b_0 [mm]	σ_y [MPa]	J_Q [kJ m^{-2}]	$\frac{10J_Q}{\sigma_y}$	B, $b_0 > \frac{10J_Q}{\sigma_y}$
In air	2S.A.1	10	10	5.25	4.75	510	778	15.25	No
9 mA cm^{-2}	2S.H9.1	10	10	5.49	4.51	510	172[a)]		

[a)]Designated as J_{QC}.

The energy for stable crack growth increased with crack length, as indicated by the positive slopes of the J–Δa curves in Figure 9 in each case, including the specimen 2S.H9.1 containing hydrogen, as for specimen type 1. However, in contrast to the results for specimen type 1, Figure 9 indicates that the tearing modulus for the specimen containing hydrogen was significantly greater than that of the specimen tested in air. This indicates that the incremental energy for stable crack growth with hydrogen was greater than for the test in air, and moreover, the energy for stable crack growth with hydrogen did increase with increasing crack length.

3.7. Plastic Correction Factor

The effect of the plastic correction factor for plastic deformation was evaluated by application to the J–Δa curves measured in air for type 1 specimens. Application of the correction factor increased the evaluated final crack size and reduced the steepness of the J–Δa curve. Nevertheless, the data for the plain-sided specimen 1P.A.0 did not intersect with the construction lines, so no fracture toughness could be evaluated. For the side-grooved specimen in air 1S.A.1, the measured fracture toughness reduced from 808 to 740 kJ m^{-2} when $2\sigma_y$ was used as the slope of the construction line. However, the application of the correction factor caused too great an increase in the crack length evaluated by the compliance method, so that the evaluated crack length was longer than the crack length measured optically for the side-grooved sample. For the plain-sided sample, the implementation of the correction factor improved the measurement and reduced the underprediction of crack length.

3.8. Fractography

Each fracture in this work was initiated by loading a notched, fatigue pre-cracked SENB specimen until fracture initiated, and subsequently, the fracture grew caused by the increased loading of the SENB specimen. A schematic of the fracture surface is

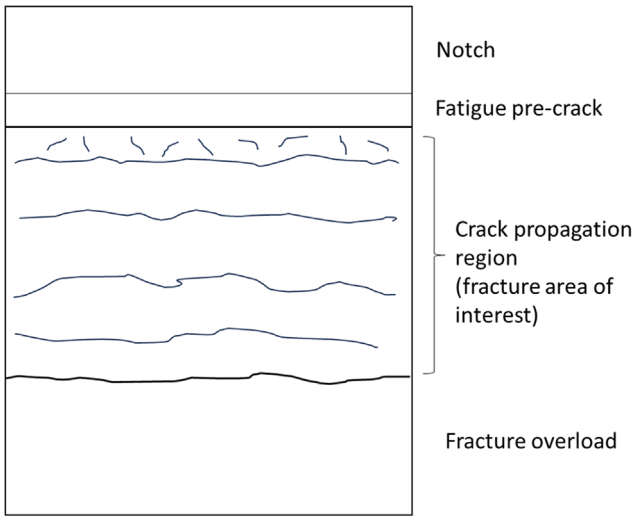

Figure 10. Schematic of the fracture surface.

presented in **Figure 10**. The fatigue pre-crack was initiated from the notch. The crack propagation region is the region of interest. This is the area of crack growth during the fracture test. Thereafter, the specimen was cooled down in liquid nitrogen and broken open to produce the region marked fracture overload in Figure 10. **Figure 11–14** present the fractographic examination of three typical specimens in the central region of the fracture surface.

The fracture growth direction was perpendicular to the elongation of the microstructure as indicated in Figure 3, which indicated that the microstructure consisted of pancake ferrite and pearlite grains, with the thin direction corresponding to the radial direction, and the long directions corresponding to the longitudinal and transverse directions. This means that the planar fracture grew alternatively through (soft) ferrite and (harder) pearlite, with a spacing of about 5 μm.

Moderate magnification views are presented in Figure 11 of a) specimen 1S.A.1 (specimen 1 of type 1 tested in air) and b) specimen 1S.H9.S2 (specimen 2 of type 1 pre-charged with hydrogen and hydrogen charged during the fracture test). In each case, the previous analysis indicated that the fracture progressed as a planar front from the top left corner toward the bottom right corner. In each case, there was a small region in the top left corner that corresponded to the region of the fatigue pre-crack, delineated by an essentially linear front from the region of stable crack growth. The fracture surface of the specimen fractured in air, Figure 11a, did not show any indication that the fracture had extended stepwise for each loading cycle during the fracture test. Furthermore, there was no fractographic feature that corresponded to the microstructure of the specimen in air. The fracture surface of the specimen tested in air, Figure 11a, showed dimples and was consistent with ductile fracture by MVC. The fracture surface of the specimen containing hydrogen, Figure 11b, also had features indicative of ductile fracture. In addition, some features extended a considerable distance perpendicular to the expected crack propagation direction that could correspond to the periodic crack advances or could correspond to features of the microstructure.

Figure 12 presents the fractography of a) specimen 1S.A.1 (specimen 1 of type 1 tested in air), showing ductile fracture by microvoid coalescence (MVC) (Figure 12a–e) and brittle fracture in the part of the specimen broken open after cooling down in liquid nitrogen (Figure 12f). The dimples had a wide range of sizes from quite small (a few microns in size, see red box in Figure 12a) to quite large (several tens of microns in diameter, see red box in Figure 12b). There were also features identified as shear dimples, see red box in Figure 12e.

Figure 13 presents the fractography of specimen 1S.H9.2 (specimen 2 of type 1 with hydrogen). Although the appearance was quite different, there was much that was similar to the fractography in air, with many dimples in appearance similar to those in air. The features marked by the red rectangle in Figure 13b were similar to the shear dimples in Figure 12e. The flat features marked by the blue squares in Figure 13a could represent a brittle fracture mode, or alternatively could be extended shear dimples. The elongated features in the white rectangle in Figure 13c are tentatively identified as fracture through pearlite. The feature identified by the white square in Figure 13c appears to be a deep dimple.

Figure 14 presents the fractography of specimen 2S.H9.2 (specimen 2 of type 2 with hydrogen). This clearly shows that the fractography was aligned in a diagonal direction across each figure, which direction was perpendicular to the expected crack

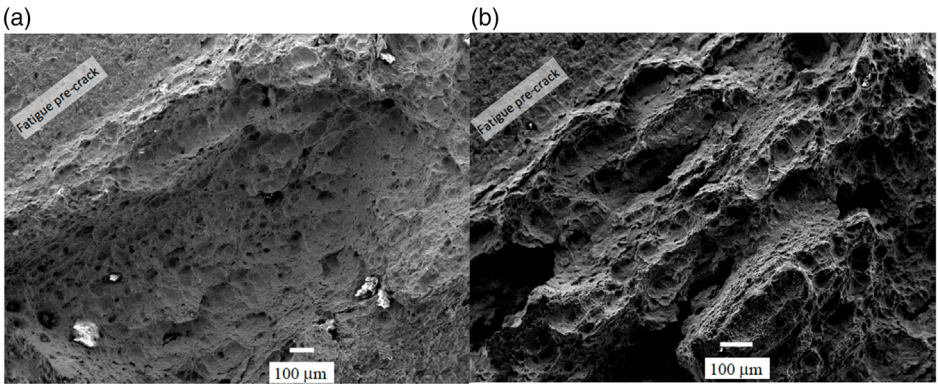

Figure 11. Moderate magnification views of a) specimen 1S.A.1 (specimen 1 of type 1 tested in air) and b) specimen 1S.H9.2 (specimen 2 of type 1 pre-charged with hydrogen and hydrogen charged during the fracture test). The fractography corresponded to the central region of the specimen.

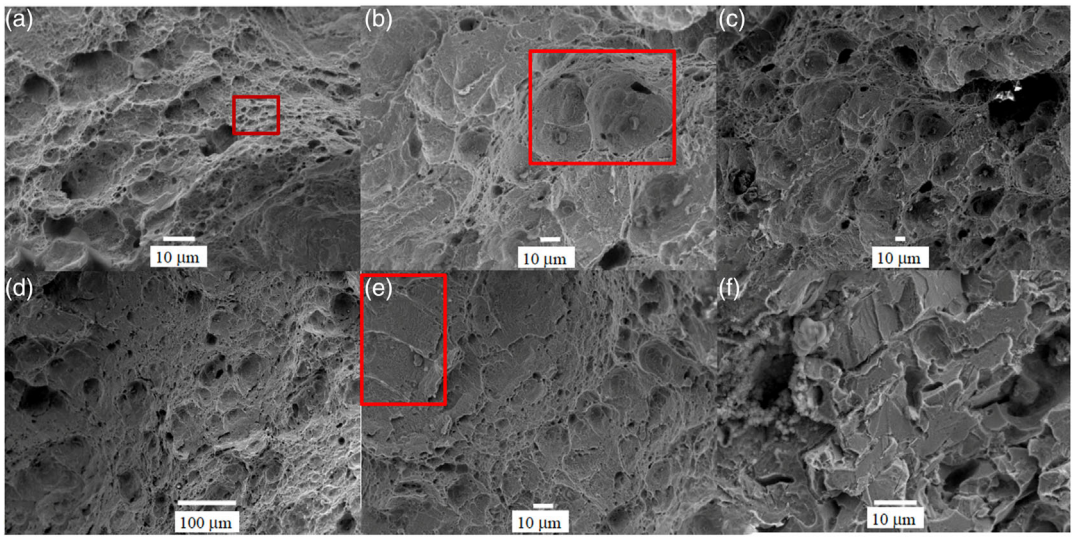

Figure 12. Fractography of specimen 1S.A.1 (specimen 1 of type 1 tested in air) showing a–e) ductile fracture by microvoid coalescence (MVC) from representative regions in the central part of the specimen, and f) brittle fracture in the part of the specimen broken open after cooling down in liquid nitrogen.

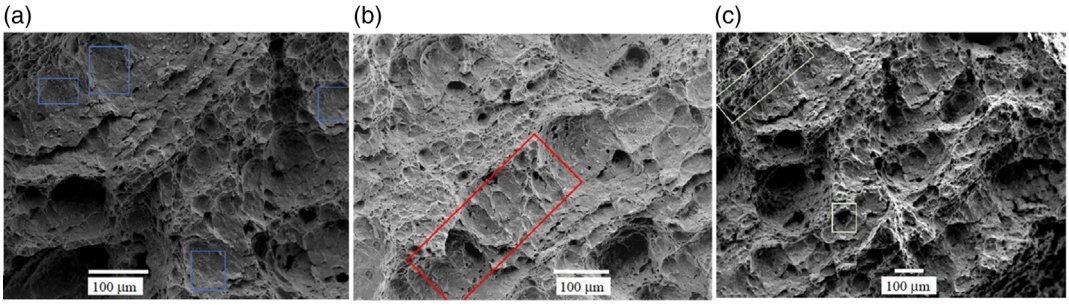

Figure 13. a–c) Fractography of specimen 1S.H9.2 (specimen 2 of type 1 with hydrogen) from representative regions in the central part of the specimen.

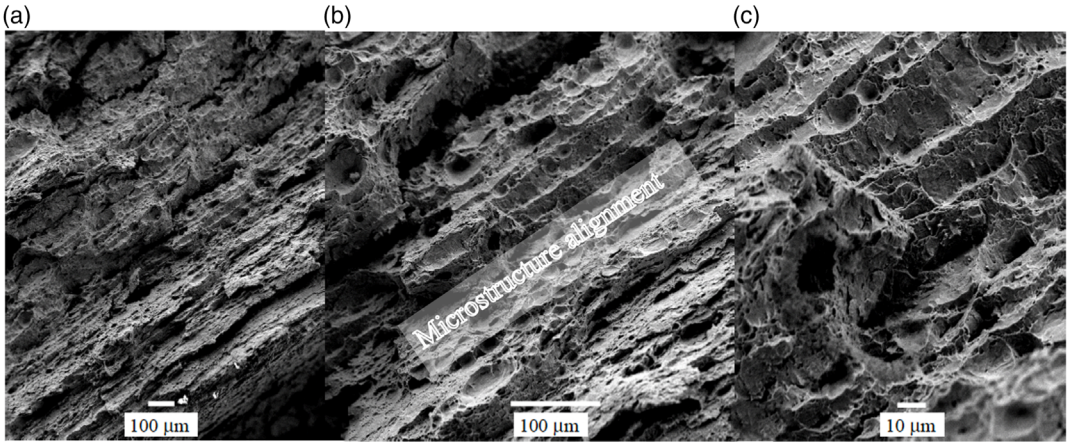

Figure 14. a–c) Fractography of specimen 2S.H9.2 (specimen 2 of type 2 with hydrogen) from representative regions in the central part of the specimen.

growth direction, which was aligned with the microstructure. Either of these reasons could be the cause of this fractographic alignment. In any case, the presence of hydrogen is the most probable cause of the difference between this fractography with hydrogen (Figure 14) and the fractography in air (Figure 12). In any case, the fractography does indicate a fracture mode with

significant ductility, possibly associated by the greater plastic flow of the ferrite in the presence of hydrogen.

There were no obvious features in the fractography corresponding to the fracture instabilities in Figure 4 and 5.

4. Discussion

4.1. Measured Values

This study produced two values of fracture toughness, J_Q, for X65 in air (590 and 778 kJ m^{-2}) and three values of fracture toughness for hydrogen-charged X65 (97, 155, and 172 kJ m^{-2}; equivalent to 150, 189, and 199 MPa$\sqrt{m}$), see Figure 8 and 9, and Table 12 and 14. The values J_Q were evaluated from the J–Δa curve at 0.2 mm crack extension, except that the value of J_Q for 1S.H9.1 and 2S.H9.1 was evaluated corresponding to 0.46 mm *CMOD* and 0.52 mm *CMOD*, respectively. In each case, there was considerable stable crack growth. In each case, the provisional values of the fracture toughness, J_Q, for hydrogen-charged specimens were considerably lower than the fracture toughness in air. Specimen 1S.H9.2 (specimen number 2, specimen type 1 with hydrogen) produced an ASTM-valid fracture toughness value of the J–integral of 155 kJ m^{-2} (equivalent to a $K_{J1C} = 189$ MPa$\sqrt{m}$) for X65 subjected to in situ hydrogen charging thought to be equivalent to a hydrogen gas pressure of 200 bar. Specimen 1S.H9.1 and 2S.H9.1 produced ASTM-valid fracture toughness values corresponding to the fracture instability occurring before the crack length reached 0.2 mm. The measured J integral for specimens 1S.H9.1 and 2S.H9.1 were 97 kJ m^{-2} (equivalent to a $K_{J1C} = 150$ MPa$\sqrt{m}$) and 172 kJ m^{-2} (equivalent to 199 MPa$\sqrt{m}$) for X65 containing hydrogen.

The energy for stable crack growth increased with crack length as indicated by the positive slopes of the J–Δa curves in Figure 8 and 9 in each case, including the specimens in air and the specimens containing hydrogen. However, the tearing modulus was different for the two specimen types. For specimen type 1, the tearing modulus for the two specimens containing hydrogen was less than that of the specimen tested in air. This indicated that the incremental energy for stable crack growth with hydrogen was lower than for the tests in air; nevertheless, the energy for stable crack growth with hydrogen did increase with increasing crack length. In contrast, for specimen type 2, the tearing modulus for the specimens with hydrogen was significantly greater than that of the specimen tested in air. This indicates that the incremental energy for stable crack growth with hydrogen was greater than that for the tests in air, and moreover, the energy for stable crack growth with hydrogen did increase with increasing crack length.

This difference in the behavior of the tearing modulus could have been caused by the specimen dimensions. For specimen type 1, the B/W ratio was equal to ½ as recommended by ASTM E1820. In contrast, for specimen type 2, $B/W = 1.0$, which was on the borderline suggested by ASTM E1820. This difference in specimen dimensions could also have been the cause for the larger fracture toughness value measured in air with type 2 specimens compared with the value measured with the type 1 specimen.

4.2. Literature Comparison

This study produced two values of fracture toughness, J_Q, for the X65 steel in air (590 and 778 kJ m^{-2}) (corresponding to 369 and 424 MPa$\sqrt{m}$) and three values for hydrogen-charged X65 (97–172 kJ m^{-2}) (corresponding to 150 and 199 MPa$\sqrt{m}$). There were two ASTM valid values of fracture toughness equivalent to $K_{J1C} = 189$ MPa$\sqrt{m}$ and $K_{J1C} = 150$ MPa$\sqrt{m}$) for X65 containing hydrogen. These values were consistent with literature values as summarized in Table 1.

The values of fracture toughness of this particular X65 were consistent with the high values in the literature of fracture toughness of X65 in air, for example, 536 kJ m^{-2} corresponding to 351 MPa$\sqrt{m}$[77] and 411 kJ m^{-2} corresponding to 308 MPa$\sqrt{m}$.[88]

The values measured for this particular X65 in hydrogen (at a hydrogen fugacity thought to be equivalent to 20 MPa) were consistent with literature values for X65 measured in gaseous hydrogen: 95–111 MPa$\sqrt{m}$ in 6.9 MPa gaseous hydrogen for (X42, X52, X60, X70, X80);[38] 105 MPa$\sqrt{m}$ for X80 exposed to 13.8 MPa gaseous hydrogen.[38]

The substantial values of the fracture toughness for this particular X65 are attributed to the steel quality. The DBNGP is 1539 km in length of the main pipeline with a small-wall thickness (12.7 mm thick). Economical construction required the use of consistent high-quality steel of high toughness.

4.3. Measured Fracture Toughness

The magnitude of a valid fracture toughness that could be measured, even when using elastic–plastic fracture toughness, was limited by the wall thickness (of 12.7 mm) of the gas transmission pipe. Specimen 1S.H9.2 (specimen number 2, specimen type 1) produced a fracture toughness value of the J integral of 155 kJ m^{-2} (equivalent to $K_{J1C} = 189$ MPa$\sqrt{m}$) for X65 subjected to in situ hydrogen charging, thought to be equivalent to a hydrogen gas pressure of 200 bar. Similarly, specimen 1S.H9.1 produced an ASTM-valid fracture toughness value of the J integral of 97 kJ m^{-2} (equivalent to $K_{J1C} = 150$ MPa$\sqrt{m}$) for X65 containing hydrogen. Table 12 indicated that the validity requirements were met for specimen 1S.H9.2. Furthermore, Figure 8 indicates that, because of the steep construction lines, the data points used for constructing the curve fit for specimen 1S.H9.2 were essentially within the J_{max}. Furthermore, the crack lengths measured with the compliance method agreed well with the optically measured crack lengths. This provided further indication of a valid measurement.

Thus, the J-integral values for 1S.H9.2 of 155 kJ m^{-2} (equivalent to $K_{J1C} = 189$ MPa$\sqrt{m}$) and for 1S.H9.1 of 97 kJ m^{-2} (equivalent to $K_{J1C} = 150$ MPa$\sqrt{m}$) represent fracture toughness values that were close to ASTM valid values for X65 subjected to in situ hydrogen charging thought to be equivalent to a hydrogen gas pressure of 200 bar. The value of fracture toughness for 2S.H9.1 of 172 kJ m^{-2} (equivalent to $K_{J1C} = 199$ MPa$\sqrt{m}$) was consistent with the other two values.

The measurements in air gave fracture toughness values that were considerably larger. These were not valid measurements according to ASTM E1820. This indicates that these measured

values need to be used with care when used for the evaluation of structural integrity. Nevertheless, the higher values indicate that the fracture toughness in air was considerably larger than in hydrogen.

The technical term "ASTM valid" merits discussion. The fracture toughness measured herein is the energy required to initiate the growth of a crack by a small amount from a fatigue pre-crack. The measured fracture toughness is initially designated as J_Q. J_Q is designated an ASTM-valid measurement of the fracture toughness, and can be designated J_{1C}, if J_Q satisfies the exacting requirements of specimen and crack size as specified by the ASTM and European standards on fracture-mechanics testing. An ASTM-valid fracture toughness is a material property characteristic of the steel and can be used for the evaluation of the structural integrity of a structure fabricated from that steel regardless of the size and complexity of the structure or the operating stresses. This means that the laboratory measurements of the fracture toughness, J_{IC}, using small laboratory specimens are directly applicable to structures in service, such as a gas transmission pipeline. If J_Q does not satisfy the exacting requirement to be an ASTM-valid measure of fracture toughness, the value of J_Q measured for a particular specimen can nevertheless be appropriately compared with values for other specimens provided that the specimens are similar. Thus, it is entirely appropriate to compare the values of J_Q measured herein with hydrogen to the values measured herein in air.

4.4. Fracture Mechanism

The fractography indicated ductile fracture in air as illustrated in Figure 11 and 12 in the region of crack propagation during the fracture toughness test. Figure 10 defines this region of the fracture surface of the specimen as examined using SEM after the fracture toughness test. Similarly, the fractography of this crack propagation region in the presence of hydrogen showed significant ductility as illustrated in Figure 13 and 14, consistent with a hydrogen-assisted plastic fracture mechanism. The fracture process was clearly ductile and assisted by hydrogen at the microscale. There was hydrogen-assisted plastic fracture during the stable ductile crack growth during the fracture test. Fracture instabilities were identified in the test in air (specimen 1P.A.0, Figure 4), which indicated that these fracture instabilities were characteristic of the fracture process of this steel in air. There is much more that can be learned about the hydrogen-assisted fracture mechanism from the fractography, and that study is ongoing.

4.5. Measurement Factors

4.5.1. Side Grooves

Initially, plain-sided SENB specimens were used for the fracture toughness tests. An example is provided in Figure 7. Each plain-sided specimen generated a steep J–Δa curve that did not intersect the 0.2 mm offset line, see Figure 7 for an example. In addition, the crack length using the elastic compliance method was significantly less than the actual physical crack length.

The literature indicated that underprediction of the crack length can occur for plain-sided specimens and that this underprediction issue can be resolved using side grooving. For example, Lee et al.[89] found that only a side-grooved specimen produced an accurate crack estimation using the elastic compliance method. Previous experiments indicated that the crack length estimated using the elastic compliance method underpredicted the actual (optically measured) crack length when plain-sided specimens were used. Minnebruggen et al.[90] found a curved crack front after fatigue pre-cracking and after the crack growth of the fracture toughness test. They found that the increased constraint at the center of the plain-sided specimen produced a curved crack front. They suggested that side grooving would be a possible solution. Gao[91] found that the absence of a side-groove caused a shear lip due to low-stress triaxiality produced near the outer surfaces of the specimen. The side grooves eliminated the low-stress triaxiality zone, allowing the crack to extend in a straight line.

In the present study, each fracture toughness test with a side-grooved specimen produced a J–Δa curve with reduced steepness that intersected the 0.2 mm offset line. The side-grooved specimen had reduced crack tunneling and hence produced a more accurate crack length estimation using the elastic compliance method.

4.5.2. Slope of the Construction Line

The slope of the construction line is $2\sigma_y$ according to the standard ASTM E1820 and can overestimate the fracture toughness of material with strain hardening. The slope of the construction line can be steeper based on the material properties and strain hardening. The ISO 12135 standard suggested the slope to be $3.75\sigma_{UTS}$. Considering the strain-hardening effect based on the material properties of the X65, the slope of the construction line was evaluated to be $4.23\sigma_y$.

The construction line significantly influenced the measured value of the fracture toughness. The fracture toughness measured in air reduced from 808 to 590 kJ m^{-2} when the slope $4.23\sigma_y$ was used for the construction line instead of $2\sigma_y$. The fracture toughness measured with in situ hydrogen charging reduced from 170 to 155 kJ m^{-2} for specimen 1S.H9.2.

4.5.3. Plastic Correction Factor

The plastic correction factor significantly increased the calculated final crack length, and reduced the steepness of the J–Δa curve. As a result, the J–Δa curve intersected the 0.2 offset line at a lower point in comparison to the uncorrected J–Δa curve. However, the crack length measured using the elastic compliance method without any correction was closer to the actual physical crack measurement. Thus, the fracture toughness measured without using any plastic correction factor was more appropriate.

4.5.4. Specimen Width

The thickness of the pipeline was 12.7 mm. It was not possible to make a flat, ASTM-E1820-compliant specimen with a width of more than 10 mm for a longitudinal crack propagating in the

radial direction. That limitation also constrained the maximum possible initial crack ligament and the J_{max} limit. Consequently, the data points between 0.15 mm exclusion line and 1.5 mm exclusion line did not fall below the J_{max} limit for each specimen except for specimen 1S.H9.2 (specimen 2 for specimen type 1) and 1S.H9.1. Thus, with these exceptions, the data points did not meet the criteria for valid data point requirements. In other words, the measured fracture toughness J_Q, was too large to meet the size requirement of the specimen according to the ASTM standard. However, the values of fracture toughness measured in this work were consistent with literature values, where the size requirement also could not be met due to the thickness limitation.[85–87]

4.5.5. Specimen Dimensions

The B/W ratio of specimen type 1 was equal to ½ as recommended by ASTM E1820. The crack length evaluated with the compliance method was in good agreement with the crack length measured optically on the specimen after the test for specimen type 1, see Table 7. This indicated that Equation (3) provided a good measure of the actual crack length. In contrast, Equation (3) did not provide a good measure of the crack length for specimen type 2, see Table 8. For this specimen type, $B/W = 1.0$, which is on the borderline suggested by ASTM E1820. This indicates that the specimen dimensions should all be consistent with the general proportion of the standard specimen according to ASTM E1820.

4.5.6. Load Control

Some considerations are appropriate about load control. The force versus *CMOD* curves in Figure 4 and 5 were measured under displacement control. Displacement control allows the force to decrease after the maximum force has been reached, and consequently allows considerable stable crack growth after the maximum force. Anderson[91] indicates that ductile fracture ensures if such data is applied to a structure under load control, and that fracture occurs at the maximum force. These conditions were evaluated in **Table 15**. These values have much less deviation than those in Table 12 and 14 and were somewhat lower. Nevertheless, the toughness values with hydrogen were considerably lower than the toughness in air, indicating a significant effect of hydrogen. Also, the crack extension for each specimen type with hydrogen was significantly larger than in air, consistent with a hydrogen-assisted plasticity fracture mechanism. These values are plotted in **Figure 15** for type 1 specimens.

Table 15. Critical values for ductile fracture under load control.

Specimen designation	Maximum force [N]	Crack extension [mm]	$J_{Q,LC}$ [kJ m^{-2}]	$K_{Q,LC}$ [MPa$\sqrt{m}$]
1S.A.1	1242	0.0709	269	249
1S.H9.1	946	0.2086	221	226
1S.H9.2	1237	0.3288	160	192
2S.A.1	5573	0.0381	254	242
2S.H9.1	4965	0.0762	132	175
2S.H9.2	4800	0.4196	363	289

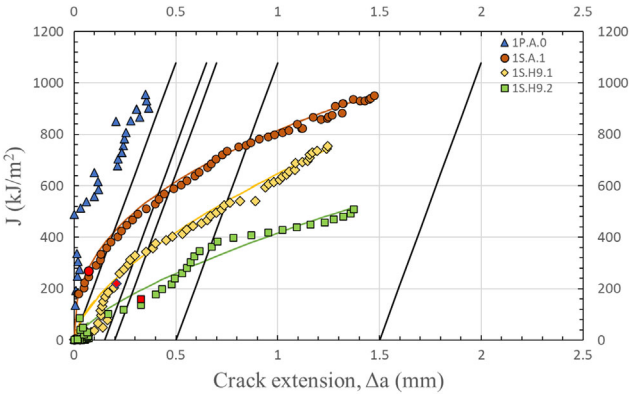

Figure 15. Plot of the $J_{Q,LC}$ values (as J_{max}) from Table 15 on the *J*–R curve (using the construction line $J = 4.23\ \sigma_y \Delta a$) for the following type 1 specimens: 1P.A.0 (plain specimen tested in air); 1S.A.1 (side-grooved specimen tested in air); 1S.H9.1 (side-grooved specimen tested with hydrogen charging); and 1S.H9.2 (side-grooved specimen tested with hydrogen charging).

5. Conclusions

Previous research indicated significant hydrogen-induced decrease of fracture toughness in gas transmission pipeline steels. Fracture toughness represents the ability of a material to resist fracture, including hydrogen-enhanced fracture initiation and propagation. The fracture toughness of X65 SENB specimens extracted from the DBNGP pipeline was measured in air and with in situ cathodic hydrogen charging. An electrolytic cell mounted on a three-point bend fixture was used to hydrogen charge each SENB specimen sufficiently long to ensure an equilibrium hydrogen concentration. The measured fracture toughness with in situ cathodic hydrogen charging was compared with the fracture toughness measured in air. The motivation of this research is to provide knowledge of the actual fracture toughness corresponding to possible hydrogen pressures in service, allowing the determination of safe operating pressures and critical crack sizes for the gas transmission pipeline transporting hydrogen.

The main conclusions were as follows. 1) There was considerable stable crack growth during the measurement of the fracture toughness of X65 in air and for hydrogen-charged specimens. 2) The provisional values of the fracture toughness, J_Q, for hydrogen-charged specimens were considerably lower than the fracture toughness values in air. 3) Specimen 1S.H9.2 (specimen number 2, specimen type 1) produced a fracture toughness value of the *J* integral of 155 kJ m^{-2} (equivalent to a $K_{JIC} = 189$ MPa$\sqrt{m}$) for X65 subjected to in situ hydrogen charging which was thought to be equivalent to a hydrogen gas pressure of 200 bar. Similarly, specimen 1S.H9.1 produced an ASTM-valid fracture toughness value of the *J* integral at instability of 97 kJ m^{-2} (equivalent to $K_{J1C} = 150$ MPa$\sqrt{m}$) for X65 containing hydrogen. 4) The fractography in the presence of hydrogen showed significant ductility, consistent with hydrogen-assisted plastic fracture. This fracture mechanism was consistent with the stable ductile crack growth during the fracture test.

Appendix

Plastic Correction Factor

Ductile deformation of the specimen during three-point bending is one reason for the underprediction of the crack length using Equation (3) and the unloading compliance method. The standard formula (Equation (3)) for estimating the crack length can produce a length shorter than the optically measured crack length. When the elastic compliance is corrected for the deformation of the specimen, there can be a significant improvement in the crack length prediction for testing in air. Steenkamp[92] also reported that the deformation of the specimen has the most significant effect on the measurements, while the effect of other factors is ≈1%. To account for the specimen plastic deflection, Dzugan et al.[93,94] proposed a correction factor that was based on that of Steenkamp, F_D, which increased with the deflection of the sample. F_D was proposed in the following form:

$$F_D = 1 - 0.665 \times \alpha \tag{21}$$

where

$$\alpha = \frac{\Delta}{2W} \tag{22}$$

where α is the deformation angle as defined in their Figure 15 and Δ is the load line displacement. The effective compliance is therefore

$$C_e = \frac{C}{\left(\frac{F_D}{F_{D0}}\right)} \tag{23}$$

where C is the experimental compliance and F_{D0} is the value of F_D at the first unloading (assumed to be fully elastic).

However, the application of the correction factor caused too great an increase in the crack length evaluated by the compliance method so that the evaluated crack length was longer than the crack length measured optically.

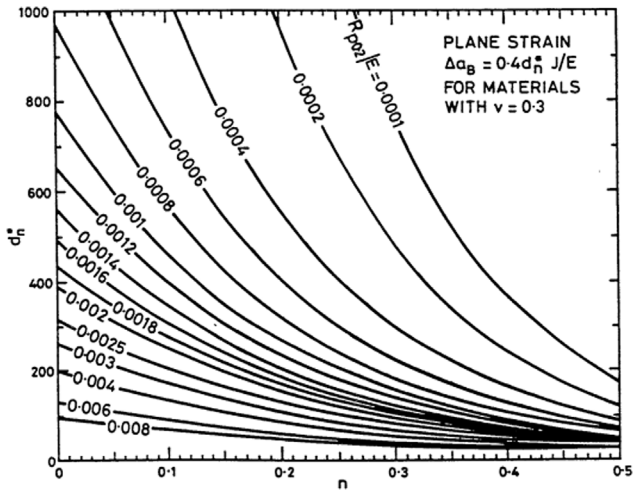

Figure A1. Determination of the blunting line coefficient, d_n^*. Reproduced with permission.[75] Copyright 1992, The European Structural Integrity Society (ESIS).

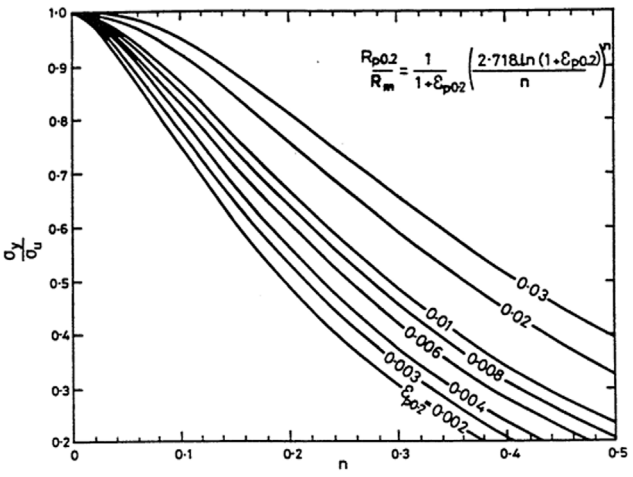

Figure A2. Determination of the strain-hardening exponent, *n*. Reproduced with permission.[75] Copyright 1992, The European Structural Integrity Society (ESIS).

Graphical Determination of d_n^* and *n*

Figure A1 allows graphical determination of d_n^*.

The hardening exponent (*n*) can be determined graphically using **Figure A2**.

Acknowledgements

This research is funded by the Future Fuels Cooperative Research Centre as research projects RP3.1-10 "Hydrogen embrittlement of pipeline steels, subcritical crack growth, 217 (formation) and critical crack growth (initiation)" and RP3.1-13 "Feasibility of the use of gas phase inhibition of hydrogen embrittlement in gas transmission pipelines carrying hydrogen," supported through the Australian Government's Cooperative Research Centres Program. JV is also supported by the Advance Queensland Industry Research Fellowship (grant no. AQIRF114-2019RD2). The authors gratefully acknowledge the cash and in-kind support from all their research, government, and industry participants. The authors also acknowledge the facilities, and the scientific and technical assistance, of the Australian Microscopy & Microanalysis Research Facility at the Centre for Microscopy and Microanalysis, The University of Queensland.

Open access publishing facilitated by The University of Queensland, as part of the Wiley - The University of Queensland agreement via the Council of Australian University Librarians.

Conflict of Interest

The authors declare no conflict of interest.

Author Contributions

M.F.W.C.: Conceptualization, Methodology, Formal Analysis, Investigation, Data Curation, Visualization, Writing—Original Draft, and Writing—Review and Editing; C.V.T.-B.: Methodology, Supervision, Writing—Review and Editing; J.H.: Writing—Review and Editing; J.V.: Methodology, Supervision, Investigation, Writing—Review and Editing; T.L.: Investigation, Writing—Review and Editing; M.B.D.: Writing—Review and Editing; T.D.: Writing—Review and Editing; K.V.: Writing—Review and Editing; L.M.: Methodology, Writing—Review and Editing;

M.R.: Writing—Review and Editing; A.K.: Writing—Review and Editing; and A.A.: Conceptualization, Supervision, Writing—Review and Editing.

Data Availability Statement

The data that support the findings of this study are available from the corresponding author upon reasonable request.

Keywords

fracture toughness, gas-transmission pipelines, hydrogen embrittlement, plastic fracture, stable crack growth, steels

Received: February 12, 2024
Revised: May 14, 2024
Published online: July 23, 2024

[1] A. Laureys, R. Depraetere, M. Cauwels, T. Depover, S. Hertelé, K. Verbeken, *J. Nat. Gas Sci. Eng.* **2022**. *101*, 104534.
[2] H. Li, R. Niu, W. Li, H. Lu, J. Cairney, Y.-S. Chen, *J. Nat. Gas Sci. Eng.* **2022**, *105*, 104709.
[3] M. L. Martin, M. J. Connolly, F. W. DelRio, A. J. Slifka, *Appl. Phys. Rev.* **2020**, *7*, 041301.
[4] Q. Liu, A. Atrens, *Corros. Rev.* **2013**, *31*, 85.
[5] J. Venezuela, Q. Liu, M. Zhang, Q. Zhou, A. Atrens, *Corros. Rev.* **2016**, *34*, 153.
[6] Q. Liu, Q. Zhou, J. Venezuela, M. Zhang, J. Wang, A. Atrens, *Corros. Rev.* **2016**, *34*, 127.
[7] A. Atrens, Q. Liu, Q. Zhou, J. Venezuela, M. Zhang, *Mater. Sci. Technol.* **2018**, *34*, 1893.
[8] M. B. Djukic, G. M. Bakic, V. S. Zeravcic, A. Sedmak, B. Rajicic, *Eng. Fract. Mech.* **2019**, *216*, 106528.
[9] S. Lynch, *Corros. Rev.* **2019**, *37*, 377.
[10] J. Hoschke, M. Chowdhury, J. Venezuela, A. Atrens, *Corros. Rev.* **2023**, *41*, 277.
[11] A. Atrens, E. Gray, J. Venezuela, J. Hoschke, M. Roethig, *JOM* **2023**, *75*, 232.
[12] *Standard Test Method for Measurement of Fracture Toughness*, E1820-20, ASTM International, West Conshohocken, PA **2020**.
[13] T. Alp, T. J. Dames, B. Dogan, *J. Mater. Sci.* **1987**, *22*, 2105.
[14] T. An, S. Zhang, M. Feng, B. Luo, S. Zheng, L. Chen, L. Zhang, *Int. J. Fatigue* **2019**, *120*, 23.
[15] H. Boukortt, M. Amara, M. Hadj Meliani, O. Bouledroua, B. G. N. Muthanna, R. K. Suleiman, A. A. Sorour, G. Pluvinage, *Int. J. Hydrogen Energy* **2018**, *43*, 19615.
[16] J. Capelle, J. Gilgert, I. Dmytrakh, G. Pluvinage, *Int. J. Hydrogen Energy* **2008**, *33*, 7630.
[17] E. V. Chatzidouros, V. J. Papazoglou, D. I. Pantelis, in *Proc. of the ASME 2011 30th Int. Conf. on Ocean, Offshore and Arctic Engineering, Volume 3: Materials Technology; Jan Vugts Symp. on Design Methodology of Offshore Structures; Jo Pinkster Symp. on Second Order Wave Drift Forces on Floating Structures; Johan Wichers Symp. on Mooring of Floating Structures in Waves*, ASME, Rotterdam, The Netherlands, June **2011**, pp. 251–260.
[18] E. V. Chatzidouros, V. J. Papazoglou, D. I. Pantelis, *Int. J. Hydrogen Energy* **2014**, *39*, 18498.
[19] E. V. Chatzidouros, V. J. Papazoglou, T. E. Tsiourva, D. I. Pantelis, *Int. J. Hydrogen Energy* **2011**, *36*, 12626.
[20] E. V. Chatzidouros, A. Traidia, R. S. Devarapalli, D. I. Pantelis, T. A. Steriotis, M. Jouiad, *Int. J. Hydrogen Energy* **2019**, *44*, 22050.
[21] Department of Energy, *U.S. Hydrogen Pipelines*, https://www.energy.gov/eere/fuelcells/hydrogen-pipelines (accessed: September 2021).
[22] K. O. Findley, M. K. O'Brien, H. Nako, *Mater. Sci. Technol.* **2015**, *31*, 1673.
[23] D. Hardie, E. A. Charles, A. H. Lopez, *Corros. Sci.* **2006**, *48*, 4378.
[24] W. Johnson, *Proc. R. Soc. Lond.* **1875**, *23*, 168.
[25] H. P. Kyriakopoulou, P. Karmiris-ObrataEski, A. S. Tazedakis, N. M. Daniolos, E. C. Dourdounis, D. E. Manolakos, D. Pantelis, *Micromachines* **2020**, *11*, 430.
[26] J. Luo, L. Zhang, L. Li, F. Yang, W. Ma, K. Wang, X. Zhao, *Nat. Gas Ind. B* **2016**, *3*, 346.
[27] B. Meng, C. Gu, L. Zhang, C. Zhou, X. Li, Y. Zhao, J. Zheng, X. Chen, Y. Han, *Int. J. Hydrogen Energy* **2017**, *42*, 7404.
[28] M. A. Mohtadi-Bonab, M. Eskandari, J. A. Szpunar, *Mater. Sci. Eng. A* **2015**, *620*, 97.
[29] J. Qu, M. Feng, T. An, Z. Bi, J. Du, F. Yang, S. Zheng, *Materials* **2019**, *12*, 2575.
[30] S. C. Silva, A. B. Silva, J. A. C. Ponciano Gomes, *Eng. Fail. Anal.* **2021**, *120*, 105081.
[31] M. Wasim, M. B. Djukic, T. D. Ngo, *Eng. Fail. Anal.* **2021**, *123*, 105312.
[32] S. Zhang, J. Li, T. An, S. Zheng, K. Yang, L. Lv, C. Xie, L. Chen, L. Zhang, *Int. J. Hydrogen Energy* **2021**, *46*, 20621.
[33] R. Garber, I. M. Bernstein, A. W. Thompson, *Metall. Trans. A* **1981**, *12*, 225.
[34] J. Shang, J. Z. Wang, W. F. Chen, H. T. Wei, J. Y. Zheng, Z. L. Hua, L. Zhang, C. H. Gu, L. Zhang, *Mater. Lett.* **2021**, *296*, 129924.
[35] L. Y. Xu, Z. Kang, Y. D. Han, L. Zhao, H. Jing, W. Zhu, *Weld. World* **2019**, *63*, 75.
[36] P. Guy, J. Capelle, in *13th Int. Conf. on Fracture 2013, ICF 2013*, Vol. *2*, Beijing, China, June **2013**, pp. 1337–1346.
[37] J. J. Hoyos, M. Masoumi, V. F. Pereira, A. P. Tschiptschin, M. T. P. Paes, J. A. Avila, *Int. J. Hydrogen Energy* **2019**, *44*, 23458.
[38] K. Xu, in *Gaseous Hydrogen Embrittlement of Materials in Energy Technologies* (Eds: R. P. Gangloff, B. P. Somerday), Woodhead Publishing, Cambridge **2012**, pp. 526–561.
[39] D. Stalheim, T. Boggess, C. San Marchi, S. Jansto, B. Somerday, G. Muralidharan, P. Sofronis, in *Proc. of the 2010 8th Int. Pipeline Conf.*, Vol. *2*, Calgary, Alberta, Canada, September–October **2010**.
[40] C. San Marchi, B. P. Somerday, K. A. Nibur, D. G. Stalheim, T. Boggess, S. Jansto in *Proc. of the ASME 2010 Pressure Vessels and Piping Division/K-PVP Conf., Volume 6, Parts A and B*, Bellevue, Washington, July **2010**.
[41] P. S. Lam, R. L. Sindelar, A. J. Duncan, T. M. Adams, *J. Press. Vessel Technol.* **2009**, *131*, 041408.
[42] S. Robinson, R. Stoltz, in *Hydrogen Effects in Metals* **1980**, pp. 987–995.
[43] G. Gutierrez-Solana, M. Elices, in *Current Solutions to Hydrogen Problems in Steels* **1982**, pp. 181–185.
[44] A. Duncan, T. Adams, P.-S. Lam, in *Proc. of the ASME 2009 Pressure Vessels and Piping Conf., Volume 6: Materials and Fabrication, Parts A and B*, Prague, Czech Republic, July **2009**, pp. 225–231.
[45] C. San Marchi, B. Somerday, *Technical reference for Hydrogen Compatibility of Materials* (No. SAND2012-7321), Sandia National Laboratories (SNL), Albuquerque, NM, and Livermore, CA **2012**.
[46] G. Álvarez, L. B. Peral, C. Rodríguez, T. E. García, F. J. Belzunce, *Int. J. Hydrogen Energy* **2019**, *44*, 15634.
[47] D. Birenis, Y. Ogawa, H. Matsunaga, O. Takakuwa, J. Yamabe, Ø. Prytz, A. Thøgersen, *Mater. Sci. Eng. A* **2019**, *756*, 396.
[48] T. T. Nguyen, H. M. Heo, J. Park, S. H. Nahm, U. N. Beak, *J. Mech. Sci. Technol.* **2021**, *35*, 1445.
[49] J. Venezuela, Q. Liu, M. Zhang, Q. Zhou, A. Atrens, *Corros. Sci.* **2015**, *99*, 98.

[50] J. Venezuela, J. Blanch, A. Zulkiply, Q. Liu, Q. Zhou, M. Zhang, A. Atrens, *Corros. Sci.* **2018**. *135*, 120.
[51] J. Venezuela, T. Hill, Q. Zhou, H. Li, Z. Shi, F. Dong, R. Knibbe, M. Zhang, M. S. Dargusch, A. Atrens, *Corros. Sci.* **2021**, *188*, 109550.
[52] H. Li, J. Venezuela, Z. Qian, Q. Zhou, Z. Shi, M. Yan, R. Knibbe, M. Zhang, F. Dong, A. Atrens, *Corros. Sci.* **2021**, *184*, 109360.
[53] H. Li, J. Venezuela, Q. Zhou, Z. Shi, M. Yan, R. Knibbe, M. Zhang, F. Dong, A. Atrens, *Mater. Sci. Eng. A* **2020**, *785*, 139343.
[54] P. Zhang, M. Laleh, A. E. Hughes, R. K. W. Marceau, T. Hilditch, M. Y. Tan, *Int. J. Hydrogen Energy* **2023**, *48*, 16501.
[55] D. Guedes, L. Cupertino Malheiros, A. Oudriss, S. Cohendoz, J. Bouhattate, J. Creus, F. ThC)bault, M. Piette, X. Feaugas, *Acta Mater.* **2020**, *186*, 133.
[56] A. Oudriss, A. Fleurentin, G. Courlit, E. Conforto, C. Berziou, C. Rébéré, S. Cohendoz, J. M. Sobrino, J. Creus, X. Feaugas, *Mater. Sci. Eng. A* **2014**, *598*, 420.
[57] G. Hachet, J. Li, A. M. Hallil, A. Metsue, A. Oudriss, J. Bouhattate, X. Feaugas, *Eng. Fract. Mech.* **2019**, *218*, 106621.
[58] C. D. Beachem, *Metall. Mater. Trans. B* **1972**, *3*, 441.
[59] H. K. Birnbaum, P. Sofronis, *Mater. Sci. Eng. A* **1994**. *176*, 191.
[60] L. Huang, D. Chen, D. Xie, S. Li, Y. Zhang, T. Zhu, D. Raabe, E. Ma, J. Li, Z. Shan, *Nat. Mater.* **2023**, *22*, 710.
[61] R. Kirchheim, *Acta Mater.* **2007**, *55*, 5129.
[62] R. Kirchheim, *Acta Mater.* **2007**, *55*, 5139.
[63] A. H. Cottrell, B. A. Bilby, *Proc. Phys. Soc. Sect. A* **1949**, *62*, 49.
[64] P. J. Ferreira, I. M. Robertson, H. K. Birnbaum, *Acta Mater.* **1998**, *46*, 1749.
[65] S. Lynch, *Corros. Rev.* **2012**, *30*, 105.
[66] Q. Liu, Q. Zhou, J. Venezuela, M. Zhang, A. Atrens, *Eng. Fail. Anal.* **2018**, *94*, 249.
[67] Q. Liu, A. D. Atrens, Z. Shi, K. Verbeken, A. Atrens, *Corros. Sci.* **2014**, *87*, 239.
[68] J. Venezuela, C. Tapia-Bastidas, Q. Zhou, T. Depover, K. Verbeken, E. Gray, Q. Liu, Q. Liu, M. Zhang, A. Atrens, *Corros. Sci.* **2018**. *132*, 90.
[69] J. Venezuela, E. Gray, Q. Liu, Q. Zhou, C. Tapia-Bastidas, M. Zhang, A. Atrens, *Corros. Sci.* **2017**. *127*, 45.
[70] Q. Liu, E. Gray, J. Venezuela, Q. Zhou, C. Tapia-Bastidas, M. Zhang, A. Atrens, *Adv. Eng. Mater.* **2018**, *20*, 1700469.
[71] E. Koren, C. M. H. Hagen, D. Wang, X. Lu, R. Johnsen, J. Yamabe, *Corros. Sci.* **2023**, *215*, 111025.
[72] A. Atrens, C. C. Brosnan, S. Ramamurthy, A. Oehlert, I. O. Smith, *Meas. Sci. Technol.* **1993**. *4*, 1281.
[73] M. Cabrini, L. Coppola, S. Lorenzi, C. Testa, F. Carugo, D. P. Bucella, T. Pastore, *Materials* **2020**, *13*, 2309.
[74] X. Li, Z. Ding, C. Liu, S. Bao, Z. Gao, *Int. J. Pressure Vessels Piping* **2020**, *187*, 104189.
[75] ESIS P2-92, in *European Structural Integrity Society-ESIS*, January **1992**.
[76] J. D. Landes, *Fatigue Fracture Eng. Mater. Struct.* **1995**, *18*, 1289.
[77] O. O. Joseph, C. A. Loto, S. Sivaprasad, J. A. Ajayi, S. Tarafder, *Eng. Fract. Mech.* **2018**, *189*, 1.
[78] L. Gajdos, in *Relations Between Mechanical and Fracture-Mechanical Properties of Linepipe Materials, NDT for Safety*, Prague, Czech Republic, November **2008**.
[79] H. Gao, W. Wang, Y. Wang, B. Zhang, C.-Q. Li, *Fatigue Fracture Eng. Mater. Struct.* **2021**, *44*, 568.
[80] J. Q. Wang, A. Atrens, D. R. Cousens, N. Kinaev, *J. Mater. Sci.* **1999**, *34*, 1721.
[81] J. Wang, A. Atrens, *J. Mater. Sci.* **2003**, *38*, 323.
[82] J. Q. Wang, A. Atrens, D. R. Cousens, C. Nockolds, S. Bulcock, *J. Mater. Sci.* **1999**, *34*, 1711.
[83] A. Atrens, J. Q. Wang, K. Stiller, H. O. Andren, *Corros. Sci.* **2006**, *48*, 79.
[84] J. Q. Wang, et al., *Acta Mater.* **1998**, *46*, 5677.
[85] O. O. Joseph, *Corrosion and Fracture Behaviour of Api-5l X65 and Micro-Alloyed Steels in Fuel Ethanol Environments*, Covenant University, Ota **2016**.
[86] S. H. Hashemi, M. Kymyabakhsh, *Amirkabir J. Mech. Eng.* **2013**, 45, 1.
[87] J.-S. Lee, J.-B. Ju, J.-i. Jang, W.-S. Kim, D. Kwon, *Mater. Sci. Eng. A* **2004**, *373*, 122.
[88] M. R. Torshizian, M. Boustani, *J. Solid Mech.* **2022**, *14*, 212.
[89] K. Lee, *Elastic-Plastic Fracture Toughness Determination Under Some Difficult Conditions*, University of Tennessee, Knoxville **1995**.
[90] K. Van Minnebruggen, D. Van Puyvelde, W. De Waele, M. Verstraete, S. Hertelé, R. Denys, *Int. J. Sustainable Constr. Des.* **2011**, *2*, 397.
[91] H. Gao, *PhD Dissertation*, RMIT University **2020**.
[92] P. Steenkamp, in *Fracture Mechanics: Eighteenth Symp.* (Ed: R. P. Reed), ASTM International, West Conshohocken, PA, pp. 583–610.
[93] J. Džugan, *Crack Lengths Calculation by Unloading Compliance Technique for Charpy Size Specimens, Wissenschaftlich-Technische Berichte/Forschungszentrum Rossendorf; FZR-385*, Juli **2003**.
[94] R. E. Link, J. Džugan, *J. Test. Eval.* **2005**, *33*, 433.